

Chapter 10

Various Applications of Lotus Metals

Abstract In this chapter, four examples of application of lotus metals are described. For heat sinks, penetrable pores are utilized to cool electronic devices. For artificial teeth, open pores are effective to let bone tissue intrude for fixation of the teeth into alveolar bones. For use of vibration–damping materials and golf putter, closed pores serve to damping effect. Thus, anisotropic pores in lotus metals contribute to such functions of products.

Keywords Biocompatibility • Golf putter • Heat sink • Implant • Vibration–damping

10.1 Nomenclature

A_b :	baseplate area of heat sink [m ²]
A_w :	cross-sectional area [m ²]
D_e :	hydraulic diameter [m]
dp_{mean} :	average diameter of pores [m]
f_g :	fin gap of groove fins [m]
f_t :	thickness of groove fins [m]
h_b :	heat transfer coefficient based on A_b [W/(m ² ·K)]
h_{dp} :	heat transfer coefficient on surface of pores [W/(m ² ·K)]
H_f :	fin height [m]
h_{fin} :	heat transfer coefficient on surface of groove fins [W/(m ² ·K)]
h_m :	average heat transfer coefficient [W/(m ² ·K)]
k :	thermal conductivity [W/(mK)]
L :	thickness of lotus type porous copper fins [m]
L_g :	length of groove fins [m]
N_t :	total number of pores
p :	porosity
Pr :	Prandtl number of fluid

Q :	heat flow [W]
Re_{dp} :	Reynolds number defined by dp
Re_{D_e} :	Reynolds number defined by D_e
R_{fi} :	thermal resistance of heat sink [K/W]
R_a :	thermal resistance of fluid [K/W]
S_f :	total surface of pores [m ²]
T_b :	temperature of baseplate [K]
T_i :	inlet temperature of fluid [K]
T_o :	outlet temperature of fluid [K]
U_i :	total fluid rate [m ³ /s]
$u_{dp\text{mean}}$:	velocity of fluid through pore [m/s]
W :	width of heat sink [m]
ΔP :	pressure drop [Pa]
η :	fin efficiency
a :	air
f :	cooling water

10.2 Heat Sink

In recent years, heat dissipation rates in power devices and laser diodes have been increasing to more than 100 W/cm² and in high-frequency electronic device, it is increasing to more than 1,000 W/cm² under the trend of miniaturization and growing capacity. Figure 10.1 shows typical cooling loads and cooling technologies compiled by Nishio [1]. When the heat flux increases, the temperature increases, and a heat flux of 100 W/cm² is as high as an equivalent heat flux from nuclear blast at 2,000 K. However, a power device or a laser diode should be kept at normal temperature level in spite of a large-heat flux of more than 100 W/cm². Therefore, novel heat sinks with high-heat transfer performance are required to cool these devices. Among various types of heat sinks, heat sinks utilizing microchannels with channel diameters of several tens of microns are expected to have excellent cooling performance because a higher heat transfer capacity is obtained with smaller channel diameters. Wei and Joshi investigated three-dimensional stacked microchannel heat sinks to enhance the cooling performance of heat sinks with microchannels [2]. Porous material with open pores is preferable for three-dimensional microchannels because of the higher surface area per unit volume and lower product cost. Bastawros and Evans investigated cellular metals as a heat transfer medium [3]. Various porous materials such as sintered porous metals, cellular metals, and fibrous composites have been investigated for heat sink applications [4, 5]. However, heat sinks using porous materials were clarified to have a high-pressure drop because the cooling fluid flow through the pores of the porous materials is complex [6].

Among the described porous materials, a lotus metal with straight pores is preferable for heat sinks due to the small pressure drop of the cooling fluid flowing

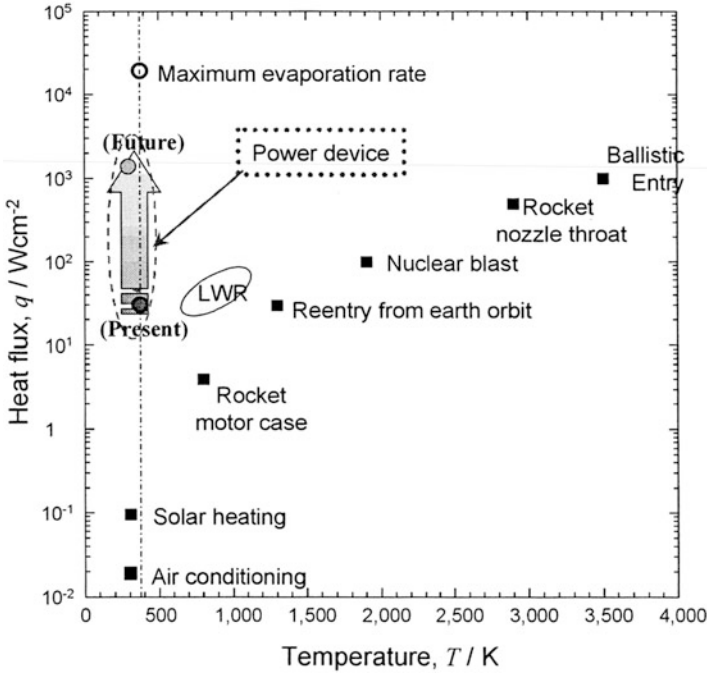


Fig. 10.1 Typical cooling loads and cooling technology [1]

through the pores. The following are the main features of lotus metals: (1) the pores are straight, (2) the pore size and porosity are controllable, and (3) porous metals can be produced with pores as small as a hundred microns in diameter. To effectively use lotus copper as a heat sink, its effective thermal conductivity must be known, by which the effect of directional pores on the heat flow must be considered. One defined perpendicular effective thermal conductivity $k_{eff\perp}$ of lotus copper as the thermal conductivity for heat flow perpendicular to the pore axis is shown in Fig. 10.2.

To predict the heat transfer capacity of a lotus copper heat sink, the correlation between heat conduction in lotus metal and heat transfer to the fluid in the pores must be considered. This correlation is generally expressed by fin efficiency. As a result of numerical analysis, the fin efficiency of the lotus copper fin was verified to be predictable by a simple straight fin model using effective thermal conductivity $k_{eff\perp}$ and the surface area ratio between the surface area of lotus copper fin and that of the straight fin [7]. Chiba et al. investigated the model for predicting the heat transfer capacity of heat sink using the lotus copper. This model takes into consideration the heat conduction in lotus copper and the heat transfer to the fluid in the pores. Finally, cooling performance of lotus copper heat sink designed by using the model for air cooling and water cooling is investigated [8].

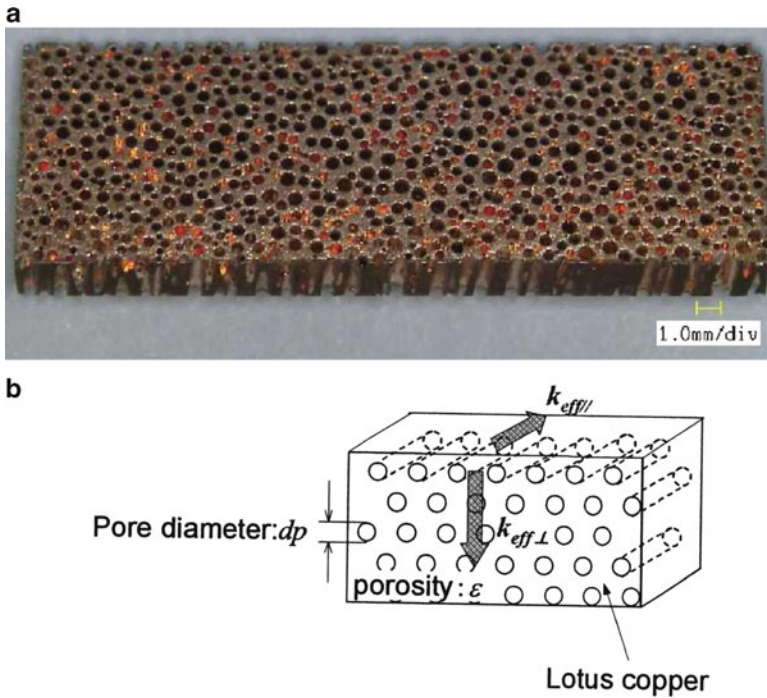


Fig. 10.2 Lotus copper with anisotropic pores: (a) outer view of lotus copper and (b) definition of thermal conductivity (Reprinted with permission from [8] © 2011 American Society of Mechanical Engineering)

10.2.1 Heat Sink for Air Cooling

Generally, a groove fin is used for cooling the power devices for air cooling or water cooling. The groove fin composes of a lot of boards connected vertically on the base. The heat transfer capacities of two types of heat sinks: (1) conventional groove fins and (2) lotus copper heat sinks, were examined. The configuration and specifications of the conventional groove fins are shown in Fig. 10.3. The conventional groove fins made of copper have a 3-mm fin gap size f_g , a 1-mm fin thickness f_t , and a 20-mm fin height H_f . The heat transfer capacity of the conventional groove fins is only derived from calculations because many experimental formulas of the fins have been established so far [9, 10]. Figure 10.4 shows the configuration of the heat sink using three lotus copper fins. W is a width. L_g is a length. Because the heat sink has 3 lotus copper fins, base area A_b of the heat sink is expressed by $3WL$.

Figure 10.5 illustrates the experimental apparatus for measuring the heat transfer capacity of heat sinks. Cooling air was blown by a blower into the test duct in which the heat sink is located. The heat sink consists of fins brazed on one side of a copper

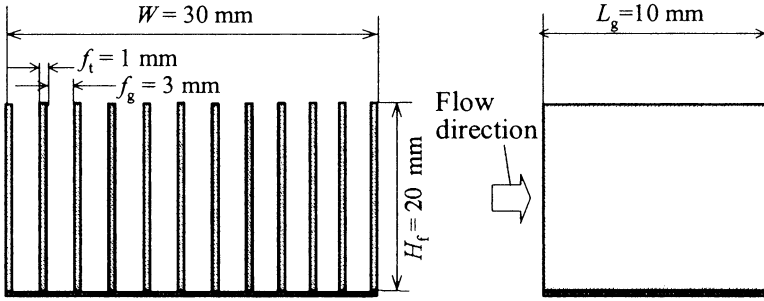


Fig. 10.3 Configuration of conventional groove fins (Reprinted with permission from [8] © 2011 American Society of Mechanical Engineering)

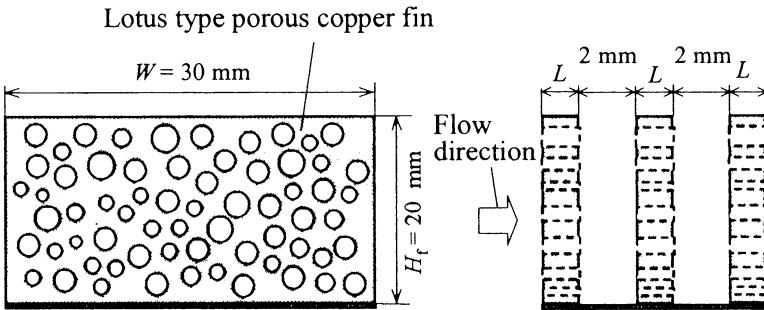


Fig. 10.4 Configuration of lotus copper heat sink (Reprinted with permission from [8] © 2011 American Society of Mechanical Engineering)

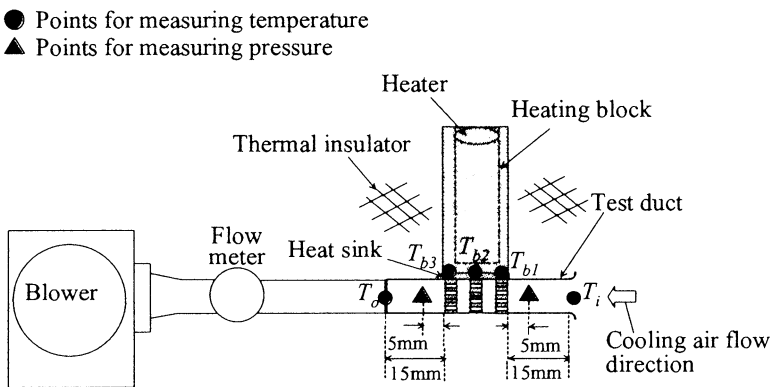


Fig. 10.5 Experimental apparatus for measuring heat transfer capacity (Reprinted with permission from [8] © 2011 American Society of Mechanical Engineering)

baseplate and the heating block with a heater soldered to the other side of the baseplate. The inlet temperature of cooling air T_i , the temperature of copper baseplates T_{b1} , T_{b2} , and T_{b3} , and the outlet temperature of the cooling air T_0 are measured by K-type thermocouples.

The heat transfer capacity by heat transfer coefficient h_b based on baseplate area A_b of the heat sink is as follows:

$$h_b = \frac{Q}{A_b(T_b - T_i)}, \quad (10.1)$$

$$Q = \rho \cdot C_p \cdot U_t \cdot (T_0 - T_i), \quad (10.2)$$

where Q is the heat input to the heat sink, ρ and C_p denote the density and the specific heat of the fluid, respectively. U_t is the total flow rate of the air through the test duct. $T_b (= (T_{b1} + T_{b2} + T_{b3})/3)$ is the mean temperature of the copper baseplate. The pressure drop between the inlet side and the outlet side of the heat sinks was measured within an experimental accuracy of $\pm 5\%$ by a pressure sensor.

Heat transfer capacity of heat sink was evaluated by using the heat transfer coefficient h_b based on baseplate surface area A_b . h_b is expressed by Eq. (10.3):

$$h_b = \frac{1}{R_{fi} \cdot A_b}, \quad (10.3)$$

where R_{fi} is the thermal resistance of the heat sink between the temperature of the baseplate and the fluid's inlet temperature. R_{fi} is expressed by

$$R_{fi} = \frac{T_b - T_i}{Q} = \frac{R_a}{1 - \exp\left(-\frac{R_a}{R_f}\right)}, \quad (10.4)$$

where R_a is the thermal resistance between the inlet and outlet of the fluid and R_f is the thermal resistance based on the logarithmic mean temperature difference between the base of the heat sink and the fluid. These thermal resistances are expressed by

$$R_f = \frac{\Delta T_m}{Q} = \frac{1}{h_{dp,mean} \cdot S_f \cdot \eta}, \quad (10.5)$$

$$\Delta T_m = \frac{T_0 - T_i}{\ln \frac{T_b - T_i}{T_b - T_0}}, \quad (10.6)$$

$$R_a = \frac{T_0 - T_i}{Q} = \frac{1}{\rho \cdot C_p \cdot U_t}, \quad (10.7)$$

where $h_{dp_{mean}}$ is the heat transfer coefficient on surface of pores S_f in the lotus copper fin. As the flow characteristics through the pores in the lotus copper fins is considered to be similar in a circle pipe, heat transfer coefficient $h_{dp_{mean}}$ is expressed by the following correlations for the circle pipe under laminar flow regime ($Re_p < 3,000$) [9]:

$$Nu_p = \frac{h_{dp_{mean}} \cdot dp_{mean}}{k_a} = 5.364 \left(1 + \{ (220/\pi) X^+ \}^{-10/9} \right)^{3/10} \times \left\{ 1 + \left(\frac{\pi/(115.2X^+)}{\left[1 + (Pr_a/0.0207)^{2/3} \right]^{1/2} \left[1 + \{ (220/\pi) X^+ \}^{-10/9} \right]^{3/5}} \right)^{5/3} \right\}^{3/10} - 1, \quad (10.8)$$

$$X^+ = \frac{L/dp_{mean}}{Re_p \cdot Pr_a}, \quad (10.9)$$

$$Re_p = \frac{u_{dp_{mean}} \cdot dp_{mean}}{\nu_a}, \quad (10.10)$$

$$u_{dp_{mean}} = \frac{U_t}{p \cdot A_w}, \quad (10.11)$$

where Nu_p and Re_p are Nusselt number and Reynolds number which are defined by average diameter for pore dp_{mean} , and ν_a and k_a are dynamic viscosity and thermal conductivity of the air, respectively. $u_{dp_{mean}}$ is the velocity of air through the pore. η is the fin efficiency of the lotus copper fin, which is calculated from the model by which lotus copper fin was assumed to be a straight fin model as follows:

$$\eta = \frac{\tanh(m \cdot H_f)}{m \cdot H_f}, \quad (10.12)$$

$$m = \sqrt{\frac{h_{dp_{mean}} \cdot \xi \cdot 2(W + L)}{k_{eff\perp} \cdot (W \cdot L)}}. \quad (10.13)$$

Pressure drop of lotus copper fin, ΔP , is expressed by the following correlation for the circle pipe under laminar flow regime:

$$\Delta P_L = \left(\frac{64}{Re_p} \cdot \frac{L}{dp_{mean}} + \zeta \right) \cdot \frac{1}{2} \rho \cdot u_{dp_{mean}}^2, \quad (10.14)$$

where ζ is the total of the pressure loss coefficient generated when the fluid flows into and out of the pores, where $\zeta = 1.4$ was assumed.

Because the conventional groove fins have often been researched so far, empirical formula for predicting their heat transfer capacity and pressure drop are established [10]. Based on the baseplate surface area, the heat transfer coefficient h_b is predicted by Eq. (10.15)

$$h_b = \frac{h_f \cdot A_f \cdot \eta}{A_b}, \quad (10.15)$$

where h_f is the heat transfer coefficient on fin surface A_f of the groove fins and is predicted by Eq. (10.16)

$$Nu_{f_g} = \frac{Nu_1 - Nu_2}{10 - Pr_a} \cdot (Pr_a - 0.71) + Nu_2, \quad (10.16)$$

$$Nu_1 = 2.80136 - 2.10514X^* + 0.411783X^{*2} + 4.11, \quad (10.17)$$

$$Nu_2 = 4.1880 - 3.14709X^* + 0.611075X^{*2} + 4.11, \quad (10.18)$$

$$X^* = \ln\left(\frac{L}{f_g} \cdot Re_{f_g} \cdot Pr_a\right), \quad (10.19)$$

where Re_{f_g} and Nu_{f_g} are the Reynolds number and the Nusselt number defined by the fin gap. u is the air velocity through the fin gap.

Pressure drop ΔP of the conventional groove fins under a laminar flow regime is expressed as follows:

$$X = \frac{L_g}{Re_{D_e} \cdot D_e}, \quad (10.20)$$

$$\Delta P = \left(f \cdot \frac{4L_g}{D_e} + \zeta\right) \cdot \frac{1}{2} \rho \cdot u^2, \quad (10.21)$$

$$f = \frac{3.44}{X^{0.5} \cdot Re_{D_e}} + \frac{24 + \frac{0.674}{4X} - \frac{3.44}{X^{0.5}}}{(1 + 0.000029 \cdot X^{-2}) \cdot Re_{D_e}}, \quad (10.22)$$

where Re_{D_e} is the Reynolds number defined by hydraulic diameter $D_e (= 4H_f f_g / (2H_f + 2f_g))$.

Chiba et al. measured the heat transfer coefficients and pressure drop using experimental apparatus of air-cooling heat sink [11]. The heat transfer coefficient h_b , based on the baseplate surface area defined by Eq. (10.3) for the experiment and Eq. (10.1) for the calculated results, respectively, is plotted as a function of the inlet velocity $u_0 (=U_i/A_w)$ in Fig. 10.6. The prediction for the lotus copper heat sink showed a good agreement with the experimental data within accuracy of $\pm 5\%$.

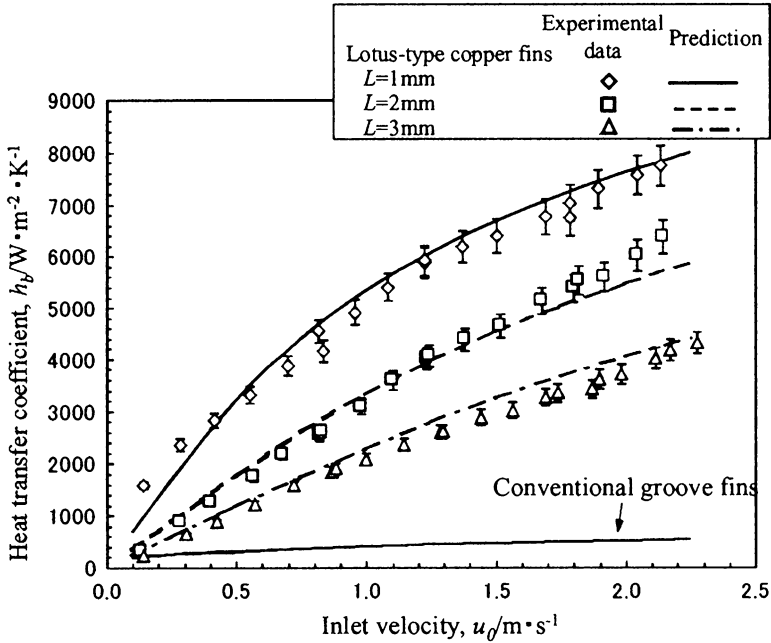


Fig. 10.6 Comparison of heat transfer coefficient h_b between experimental and predicted data (Reprinted with permission from [8] © 2008 Elsevier B.V.) (Reprinted with permission from [8] © 2011 American Society of Mechanical Engineering)

The experimental data for lotus copper heat sink with thickness $L = 1\text{ mm}$ showed a very large-heat transfer coefficient of $5,000\text{ W}/(\text{m}^2\text{ K})$ under an inlet velocity of 1.0 m/s , which is 13.2 times higher than that for the conventional groove fins.

The pressure drop ΔP in lotus copper heat sinks is plotted as a function of the inlet velocity to heat sink u_0 in Fig. 10.7. The predicted pressure drop of lotus heat sink, denoted by $3\Delta P_L$, shows a good agreement with the experimental data within accuracy of $\pm 10\%$. Comparing the pressure drop among all of heat sinks at the inlet velocity u_0 of 1.0 m/s , the experimental data show that the pressure drop of lotus copper heat sink with thickness $L = 3\text{ mm}$ is 13.5 times higher than that of the conventional groove fins.

The heat transfer coefficient h_b is shown as a function of the pumping power $\Delta P \cdot U_t$ that is defined by the product of the pressure drop ΔP and the total flow rate U_t (Fig. 10.8). A comparison of the heat transfer coefficient among all lotus copper heat sinks under a pumping power of 0.02 W revealed that the experimental data for lotus copper heat sink with thickness of 1 mm are 11.3 times higher than those for the conventional groove fin.

In summary, the thinner the lotus copper fin is, the higher is the heat transfer capacity of a lotus copper heat sink under identical pressure drop and identical pumping power. It is preferable that the thickness of the lotus copper is small when a lotus copper fin is used for heat sink.

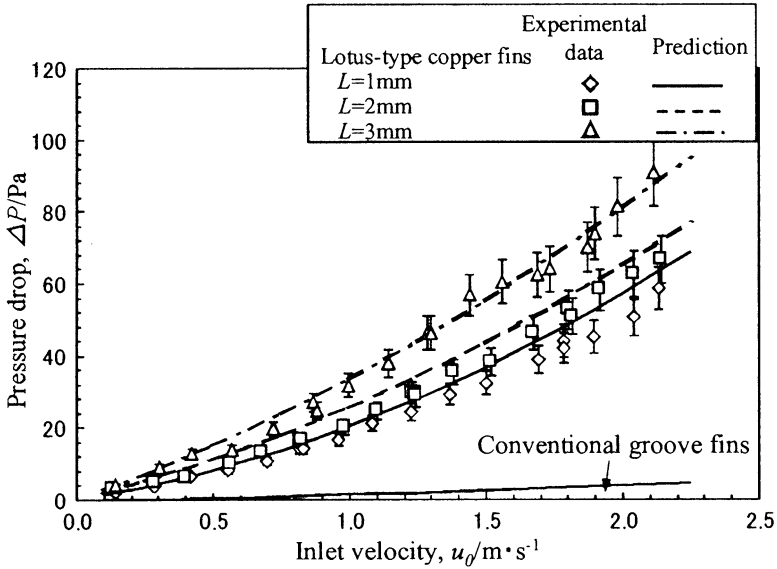


Fig. 10.7 Comparison of pressure drop ΔP between experimental and predicted data (Reprinted with permission from [8] © 2011 American Society of Mechanical Engineering)

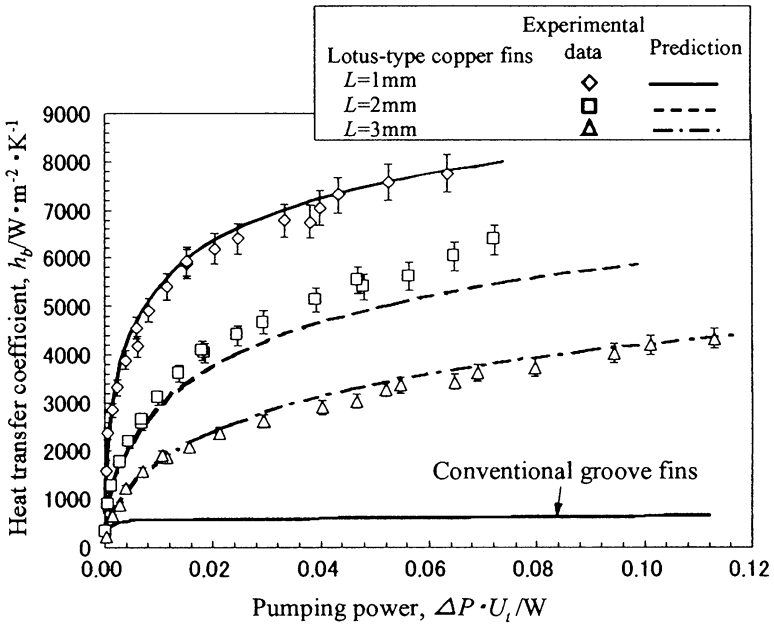


Fig. 10.8 Comparison of heat transfer coefficient h_b as a function of pumping power $\Delta P \cdot U_t$ (Reprinted with permission from [8] © 2011 American Society of Mechanical Engineering)

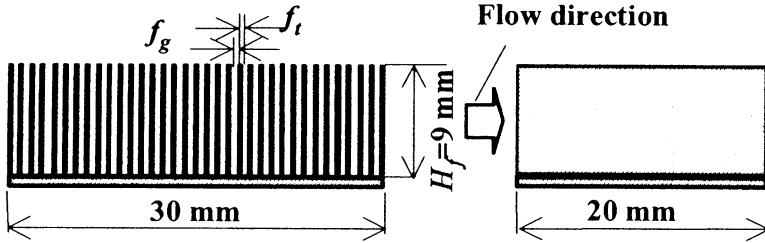


Fig. 10.9 Configuration groove fins and microchannel copper heat sink (Reprinted with permission from [8] © 2011 American Society of Mechanical Engineering)

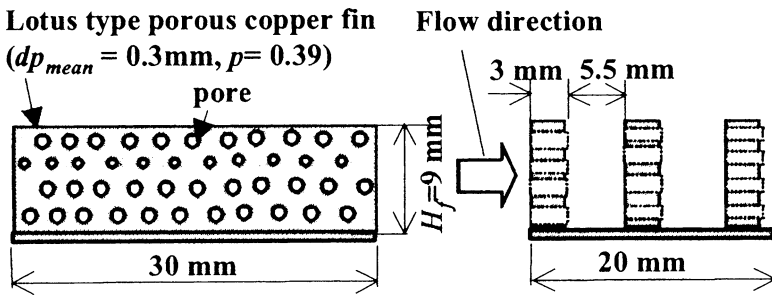


Fig. 10.10 Lotus copper heat sink for water cooling (Reprinted with permission from [8] © 2011 American Society of Mechanical Engineering)

10.2.2 Heat Sink for Water Cooling

The heat transfer capacity of three types of heat sinks for water cooling with conventional groove fins, groove fins with smaller fin gap (microchannel), and lotus copper were investigated. The configuration and the specifications of the conventional groove fins and microchannels are shown in Fig. 10.9. The conventional groove fins have fin gap of 3 mm and fin thickness of 1 mm. The microchannels have fin gap of 0.5 mm and fin thickness of 0.5 mm. The heat transfer capacity of the conventional groove fins is only for calculation. On the other hand, the configuration of lotus copper heat sink for water cooling is shown in Fig. 10.10. The heat sink has three pieces of lotus copper fins with the thickness of 3 mm along the flow direction. The lotus copper fins have pores with the mean diameter of 0.3 mm and the porosity of 39 %. Experimental apparatus for measuring the heat transfer capacity of heat sink is shown in Fig. 10.11. A cooling water was circulated through a filter and the test duct in which the heat sink is located. The circulator has a pump and water-cooling equipment. The heat sink consists of fins that are brazed on one side of a copper baseplate. The heat sink block with a heater was soldered on the other side of the baseplate. Inlet temperature of cooling

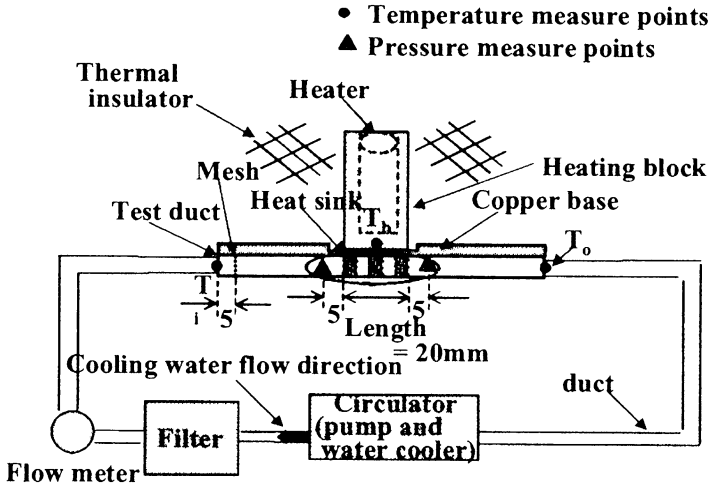


Fig. 10.11 Experimental apparatus for measuring heat transfer capacity for water cooling (Reprinted with permission from [8] © 2011 American Society of Mechanical Engineering)

water T_i , a temperature of copper baseplate T_b , and outlet temperature of cooling water T_o were measured by K-type thermocouples. From the measurement result, heat transfer coefficient was calculated by Eq. (10.1). The pressure drop between the inlet and the outlet of the fins of every heat sink was measured.

The heat transfer coefficients based on baseplate surface area A_b defined by Eq. (10.1) for experiment and Eq. (10.3) for prediction, respectively, are plotted for all of heat sinks as a function of the inlet velocity to the heat sinks u_0 in Fig. 10.12. The prediction for lotus copper heat sink showed good agreement with the experimental data within an accuracy of $\pm 15\%$. The experimental data of lotus copper heat sink showed very large-heat transfer coefficient of $80,000 \text{ W}/(\text{m}^2 \text{ K})$ under the velocity u_0 of 0.2 m/s that is 1.7 times higher than that of the microchannels and 6.5 times higher than that of the conventional groove fins.

The value of pressure drop of all the heat sinks is compared in Fig. 10.13 as a function of u_0 . The predicted pressure drop of lotus copper heat sink showed good agreement with the experimental data within an accuracy of $\pm 5\%$. Comparing the pressure drop among all of the heat sinks under the velocity u_0 of 0.2 m/s , the experimental data of the lotus copper heat sink is 2.5 times higher than that of the microchannels and 38 times higher than that of the conventional groove fins. The heat transfer coefficient h_b is shown as a function of pumping power that is defined by a product of a flow rate U_t and ΔP is shown in Fig. 10.14. Comparing the heat transfer coefficients among all of the heat sinks under the pumping power of 0.01 W , the experimental data of lotus copper heat sink is 1.3 times higher than that of the microchannels and 4 times higher than that of the conventional groove fins. Thus, the use of lotus metals is the most superior for the heat sinks of air cooling and water cooling.

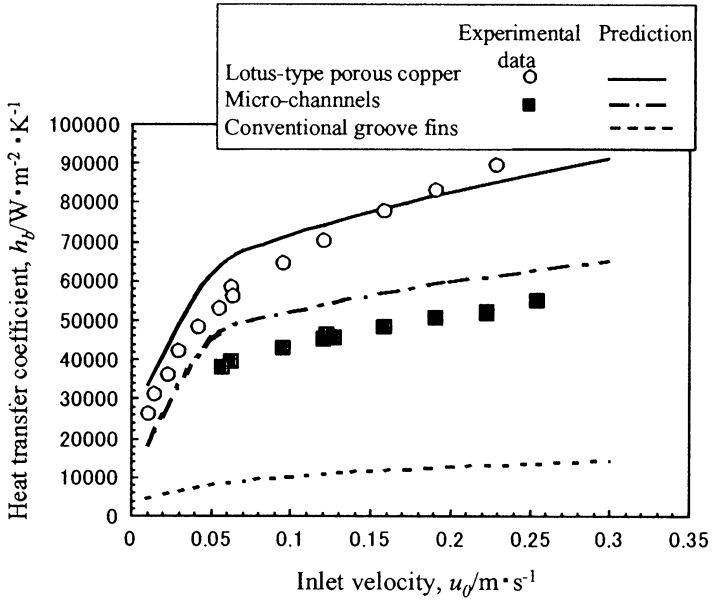


Fig. 10.12 Comparison of heat transfer coefficient h_b between experimental and predicted data (Reprinted with permission from [8] © 2011 American Society of Mechanical Engineering)

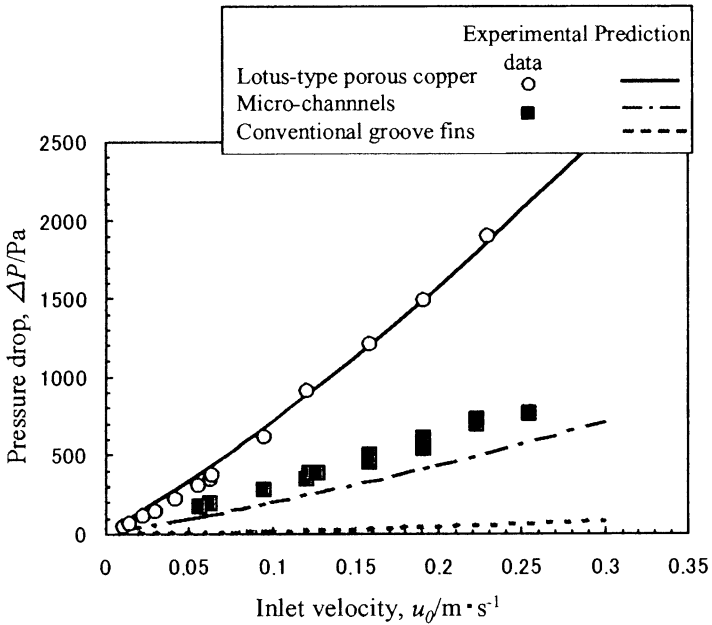


Fig. 10.13 Comparison of pressure drop ΔP between experimental and predicted data (Reprinted with permission from [8] © 2011 American Society of Mechanical Engineering)

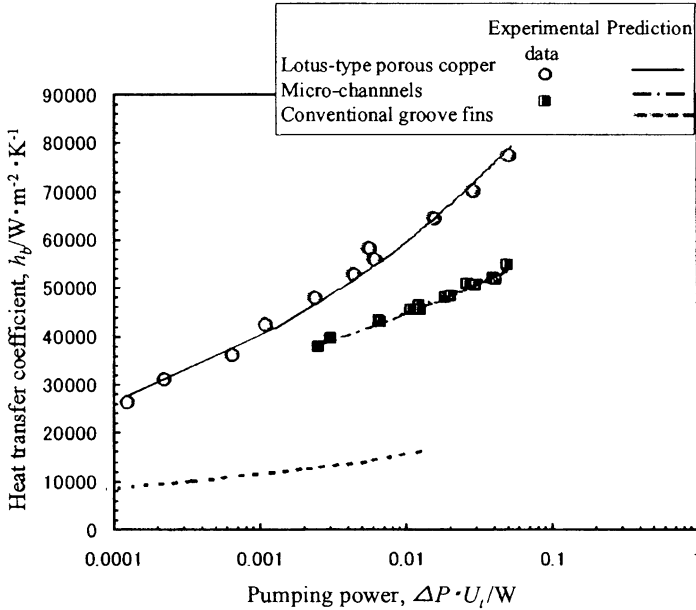


Fig. 10.14 Comparison of heat transfer coefficient h_b as a function of pumping power $\Delta P \cdot U_t$ (Reprinted with permission from [8] © 2011 American Society of Mechanical Engineering)

10.3 Vibration–Damping Materials

Nowadays, the demand for high-damping materials is increasing in various fields such as aerospace, transformation, and manufacturing industries. Also in an environmental problem, high-damping materials play an important role on the reduction of noise. Therefore, various damping materials have been produced and developed so far [12]. It is known that porous materials such as cellular materials and foamed metals show a high-damping capacity [13]. The combination of the two characteristics of lightness in weight and high-damping capacity makes porous metals more attractive. However, the mechanical strength of conventional porous materials is quite low due to their complicated porous structure, and this weak mechanical strength limits their applications. The strength of lotus metals is superior to that of conventional porous materials. If lotus metals show a high-damping capacity as well as the conventional porous materials, lotus metal can be a new high-damping material combining two characteristics of lightness in weight and high strength. Xie et al. investigated the damping capacity of lotus magnesium, which was measured by hammering–vibration–damping tests [14].

Figure 10.15 shows the schematic drawing of the apparatus for the hammering–vibration–damping method. The disc-shaped specimen is hanged with two strings, and the stainless steel sphere of 10 mm in diameter and 4 g in weight is also hanged with a string. They lift the sphere up to 20 mm in height and release it. The swung

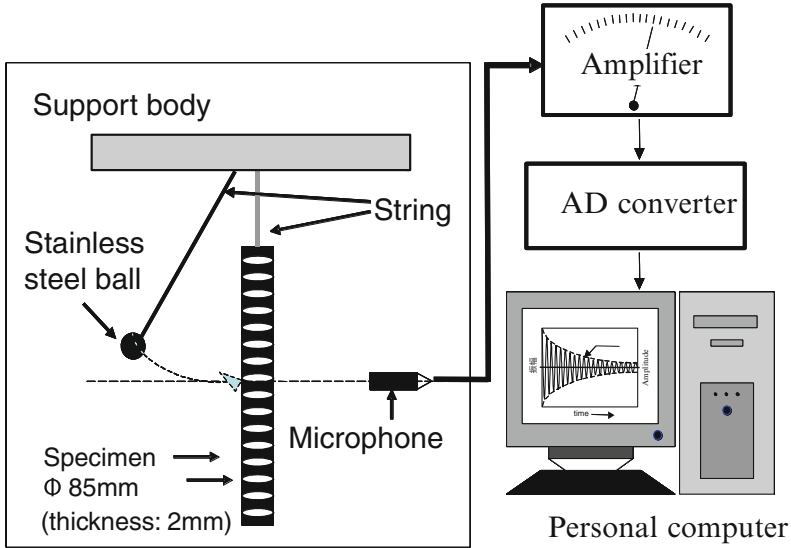


Fig. 10.15 Schematic illustration showing the measurement system for the damping capacity (attenuation coefficient) by hammering–vibration–damping tests (Reprinted with permission from [14] © 2005 Elsevier B.V.)

sphere hits the center of the disc-shaped specimen and excites the free vibration. The acoustic microphone detected the amplitude of the specimen vibration through the acoustic waves. The AD converter transforms the analog signals obtained with the microphone into the digital signals, where the sampling frequency of the AD converter is 42 kHz. Figure 10.16 shows the vibration–damping curves of the nonporous and lotus magnesium with the porosity of 44.4 % after excitation of the vibration. While for nonporous magnesium, the amplitude of a free vibration gradually decreases with increase in time, the amplitude decreases steeply for lotus magnesium. Figure 10.17 shows the Fourier transforms of the vibration–damping curves of nonporous and lotus magnesium. The Fourier transforms of nonporous magnesium possess one large peak and two small peaks, which indicate that a hammering mainly excites the fundamental mode of resonance vibrations. On the other hand, many peaks observed for lotus magnesium indicate that a hammering excites various resonant-vibration modes.

Here, one considers a material vibration at a resonant frequency by cyclic external force. When the external force is removed, the resonant-vibration damps gradually. Then, the amplitude of a damping vibration, $A(t)$, can be expressed as

$$A(t) = A_0 \exp(-\alpha t + i2\pi f_r t), \quad (10.23)$$

where t denotes the time after removal of an external force, A_0 denotes the amplitude at $t = 0$, and f_r denotes a resonant frequency. α denotes the attenuation (damping) coefficient, which depends on the damping capacity of materials.

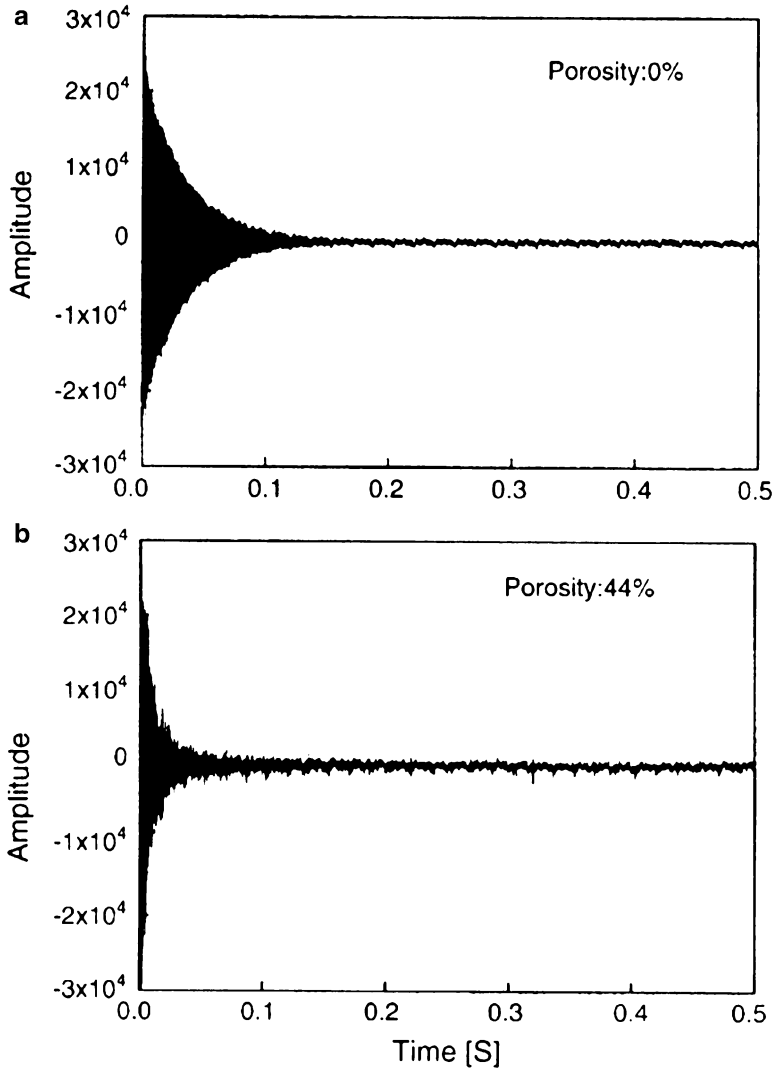


Fig. 10.16 Vibration–damping curves of (a) nonporous magnesium (porosity 0 %) and (b) lotus magnesium with the porosity of 44.4 % (Reprinted with permission from [14] © 2005 Elsevier B.V.)

For lotus magnesium, various vibration modes are excited, and therefore they cannot obtain the attenuation coefficient by fitting Eq. (10.23) to the vibration–damping curve. To determine α in such a case, they picked up the maximum value of the positive amplitude of the damping curve and fitted the equation

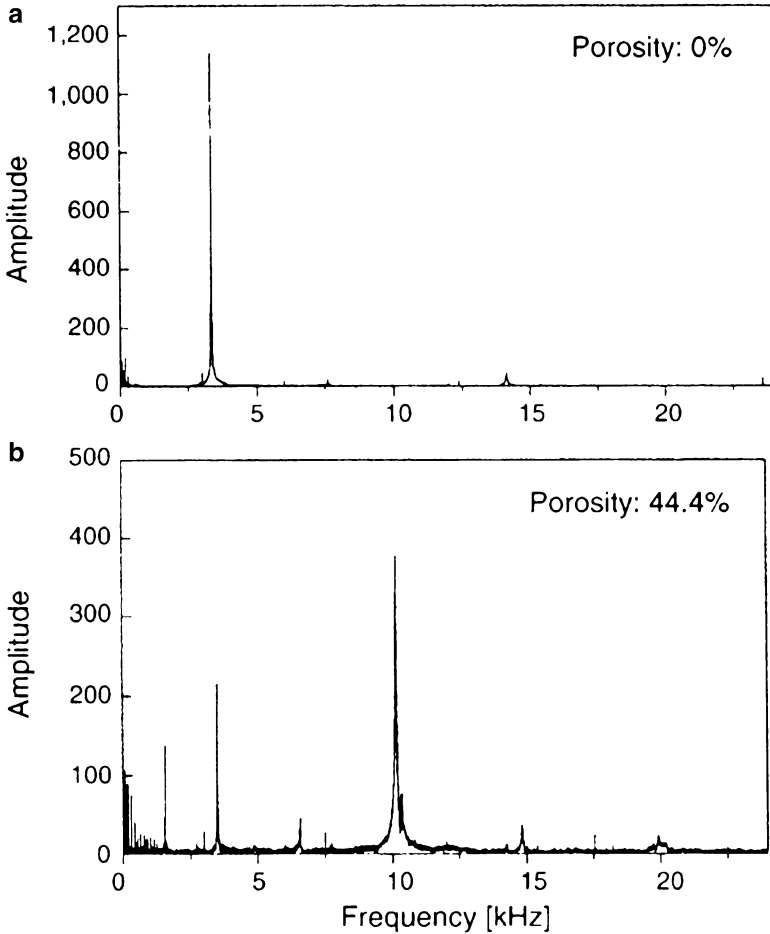


Fig. 10.17 The Fourier transforms of the vibration–damping curves of (a) nonporous magnesium (porosity 0 %) and (b) lotus magnesium with the porosity of 44.4 % (Reprinted with permission from [14] © 2005 Elsevier B.V.)

$$A(t) = A_0 \exp(-\alpha t) + C \quad (10.24)$$

to the amplitude and obtained the apparent attenuation coefficient of lotus magnesium, where C denotes a fitting coefficient. Figure 10.18 shows the vibration–damping curve of lotus magnesium of 44.4 % in porosity and the curves obtained by fitting Eq. (10.24) to the vibration–damping curves. Figure 10.19 exhibits the porosity dependence of the apparent attenuation coefficient of lotus magnesium. The apparent attenuation coefficient increases with increase in porosity.

When a resonant vibration of a material at a resonant frequency damps, the attenuation coefficient depends on the resonant frequency and intrinsic internal friction, Q^{-1} :

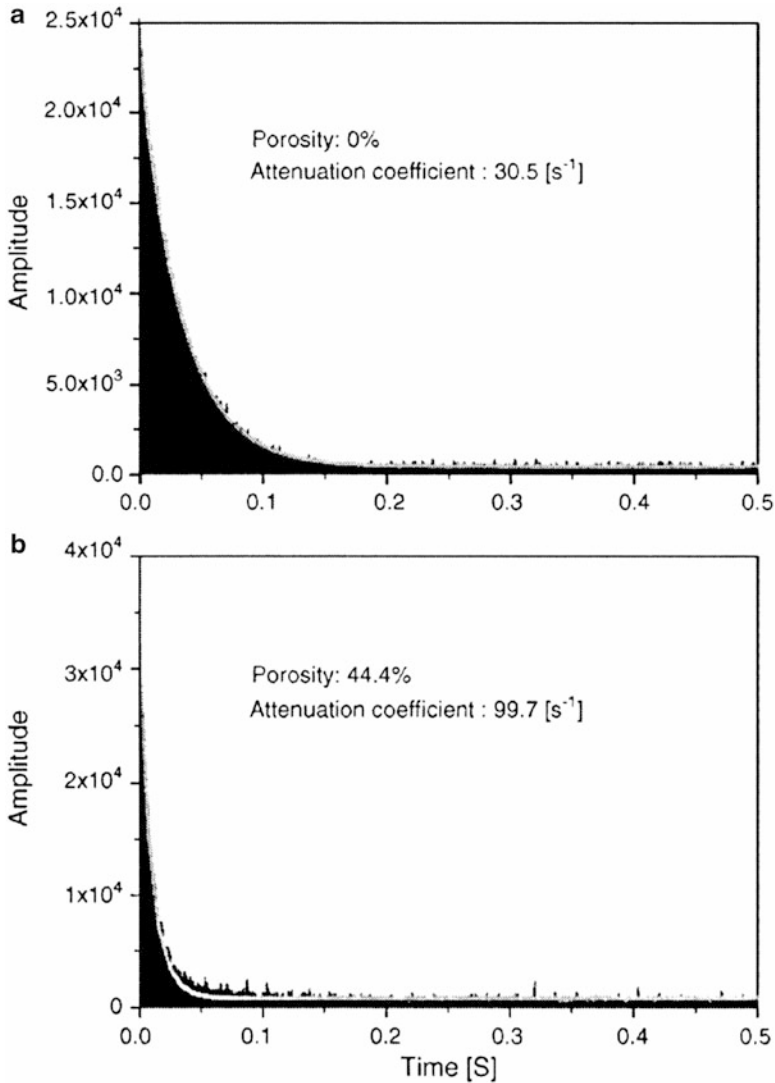


Fig. 10.18 The vibration–damping curves of (a) nonporous magnesium and (b) lotus magnesium with the porosity of 44.4 %. The curves were obtained by fitting Eq. (10.24) to the vibration–damping curves (Reprinted with permission from [14] © 2005 Elsevier B.V.)

$$\alpha = \pi f_r Q^{-1}. \quad (10.25)$$

The measurement of the internal friction of lotus copper [15] revealed that the internal friction hardly depends on porosity at room temperature. Therefore, one can assume that Q^{-1} of lotus magnesium is independent of its porosity and

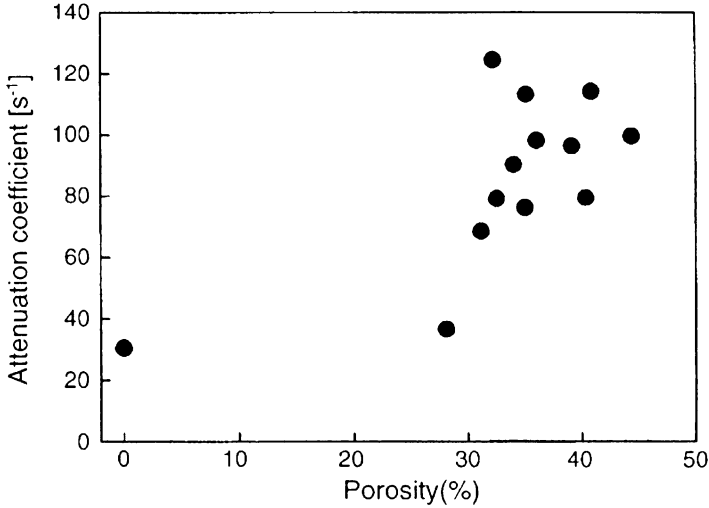


Fig. 10.19 Porosity dependence of the attenuation coefficients of lotus magnesium, which was measured by hammering–vibration–damping tests (Reprinted with permission from [14] © 2005 Elsevier B.V.)

resonant-vibration mode, i.e., the attenuation coefficient depends only on the resonant frequency. The resonance frequency depends on the elastic constants, density, and dimension of the specimen. The presence of the pores decreases the frequency of the resonant-vibration modes, and therefore, the resonant frequency of the fundamental mode of the lotus magnesium of 44.4 % in porosity is lower than that of nonporous magnesium. If a hammering excites only fundamental mode, the attenuation coefficient of lotus magnesium is smaller than that of nonporous magnesium. However, in fact, various vibration modes are excited for lotus magnesium, which affects the apparent attenuation coefficient. In order to discuss the effect of such a mode excitation, they picked up the vibration–damping curves consisting of specific frequency using Fourier transforms technique. Figure 10.20 shows the vibration–damping curve of a specific vibration mode, where the curves containing the overall frequencies are shown for comparison. The vibration of nonporous magnesium mainly consists of one resonant-vibration mode, and the apparent attenuation coefficient mainly depends on the resonant frequency of 3.3 kHz. On the other hand, the vibration of the lotus magnesium of 44.4 % in porosity mainly consists of various resonance modes, and therefore, the amplitude of the overall vibration disperses to the various resonance modes. At $t = 0$, the amplitude of resonance mode of 10.2 kHz is larger than that of 1.6 kHz. However, the resonant vibration of 10.2 kHz damps faster than that of 1.6 kHz. For lotus magnesium, the frequencies of most of excited vibrations are higher than that of fundamental mode of nonporous magnesium, and the resonance modes of high frequencies are dominant in the apparent attenuation coefficient. Therefore, the attenuation coefficients of lotus magnesium are larger than that of nonporous magnesium.

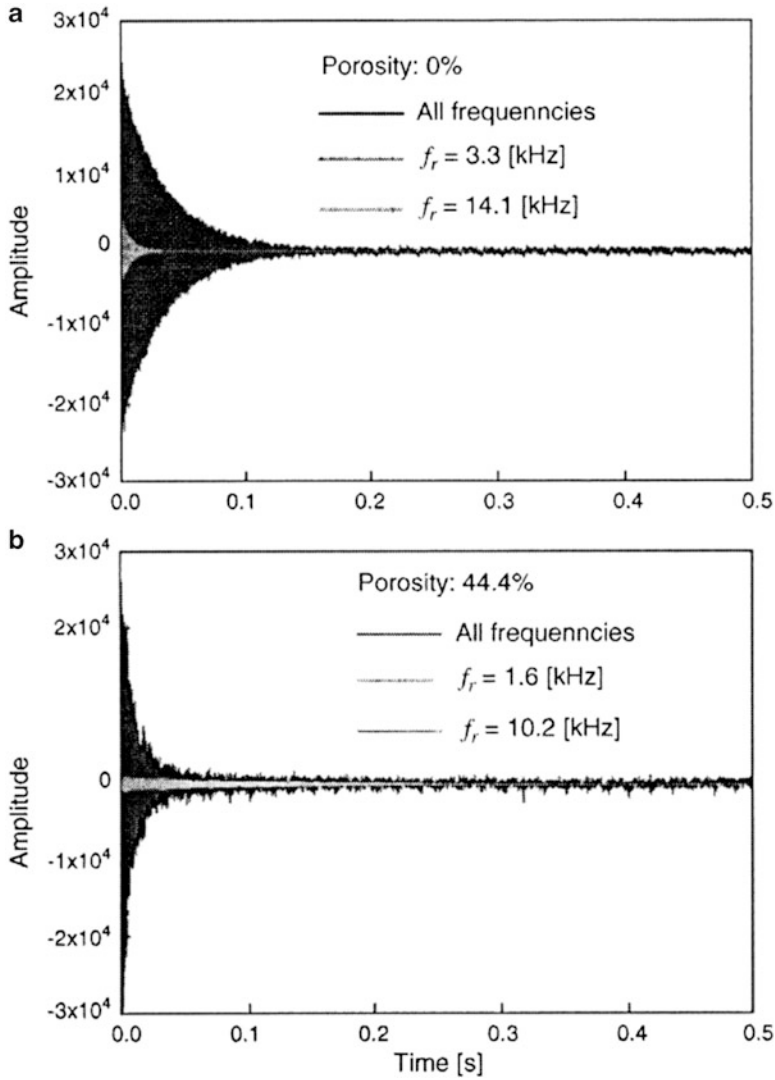


Fig. 10.20 Vibration–damping curves of (a) nonporous magnesium and (b) lotus magnesium with the porosity of 44.4 %. (a) *Black line* denotes the vibration–damping curve consisting of the overall frequencies. *Dark-gray* and *light-gray lines* denote the damping curves of the resonant modes of 3.3 and 14.1 kHz, respectively. (b) *Black line* denotes the vibration–damping curve that consists of the overall frequencies. *Dark-gray* and *light-gray lines* denote the damping curves of the resonant modes of 10.2 and 1.6 kHz, respectively (Reprinted with permission from [14] © 2005 Elsevier B.V.)

In order to compare the vibration–damping capacity of lotus magnesium with those of various metals and alloys, Xie et al. measured the attenuation coefficients of various metals and alloys using the hammering–vibration–damping method.

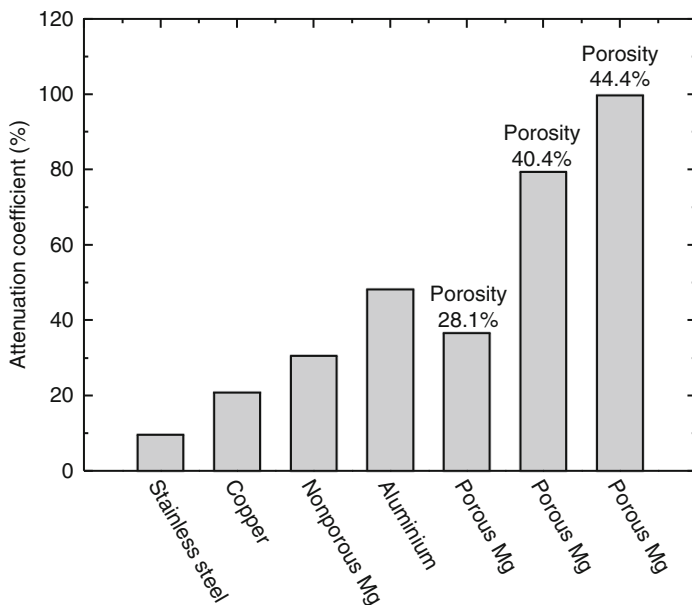


Fig. 10.21 Attenuation coefficients of nonporous aluminum, copper, stainless steel magnesium, and lotus magnesium with different porosity (Reprinted with permission from [16] © 2006 Elsevier Ltd)

Figure 10.21 shows the attenuation coefficients of nonporous aluminum, copper, and stainless steel. The attenuation coefficients of lotus magnesium are larger than those of nonporous aluminum, copper, and stainless steel which indicates that lotus magnesium is newly considered as desirable candidate of high-damping material.

10.4 Golf Putter

Usually, new materials have been first adopted to produce sporting goods, weapons, space materials, etc., whose costs can be almost disregarded. Since the lotus metals are rather new materials, commercialization of lotus metals to sporting goods is reasonable. In 2002, lotus copper was for the first time commercialized as golf putter manufactured by Ryobi Corporation in Japan.

Nonporous copper, lotus copper, and resin were put into the putter flange as inserted materials. The vibration–damping capacity of the inserted materials such as nonporous copper, lotus copper, and resin was investigated [16]. Three damping curves were measured by hammering–vibration–damping method. Figure 10.22 shows the configuration of putter head, measurement apparatus of damping, the damping results, and the attenuation coefficients. The results

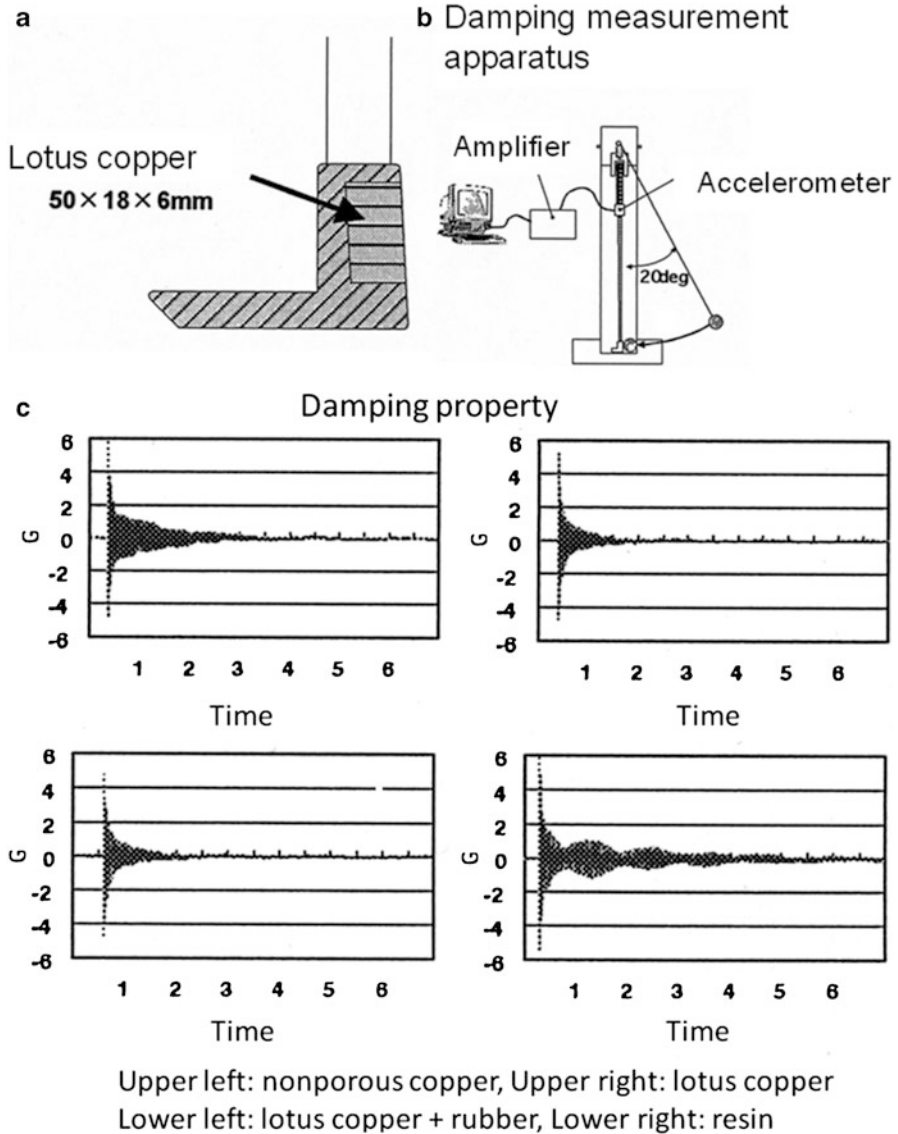


Fig. 10.22 (a) Configuration of putter head, (b) damping measurement apparatus, (c) the damping property; the vertical axis shows the amplitude and the transversal axis shows the time (upper left, nonporous copper; upper right, lotus copper; lower left, lotus copper inserted by the rubber; lower right, resin)

exhibited that lotus copper had superior damping capacity, and thus, the company decided to commercialize the putter with lotus copper. It is said that feeling of a golf putter hitting a ball is mild. Figure 10.23 shows the golf putter whose central



Fig. 10.23 Golf putter whose central part is made of lotus copper. This putter exhibits superior vibration–damping capacity. Players feel soft to hit a ball (Reprinted with permission from [16] © 2006 Elsevier Ltd)

part is made of lotus copper: the porosity is 40 % and the pore size is about 100 μm in diameter.

10.5 Medical Devices

Porous metallic biomaterials have been developed for the reconstruction of hard tissues since those provide obvious advantages over typical monolithic implants. One of these is the possibility to match the mechanical properties to those of bone to prevent stress shielding and loosening of the implant. Metals and alloys processed to create a porous structure by means of powder metallurgy processes [17–19], solid free-form fabrication [20], or vapor deposition of the metal, i.e., tantalum on vitreous polymer network, have been shown to enhance the bone ingrowth and osseointegration [21–24]. In addition, a porous surface improves the mechanical interlocking between the host bone and the implant biomaterial [25], reinforcing the stability of the implant by biological fixation. Thus, application of the porous metallic biomaterials to medical devices has been increasingly expected.

10.5.1 *In Vitro Cytocompatibility of Lotus Ni-Free Stainless Steel*

Three kinds of stainless steels containing different contents of chromium were employed in the investigation of in vitro cytocompatibility by Alvarez et al. [26]: Fe-25Cr-1N, Fe-23Cr-2Mo-1N, and AISI 446-1N [composition (wt.)]. Beside

AISI 316L stainless steel was also tested for comparison. Lotus stainless steels were fabricated using continuous zone melting technique. In order to alloy the samples with nitrogen, a high temperature solution nitriding treatment was applied. The high temperature solution nitriding treatment was carried out by sealing the plate samples into a quartz tube of $20 \text{ mm}\phi \times 170 \text{ mm}$ in a nitrogen atmosphere of 0.07 MPa. The encapsulated samples were heat-treated at $1,100 \text{ }^\circ\text{C}$ for 604.8 ks and then quenched into a water bath. After this heat treatment the stainless steel samples of originally ferritic structure become austenitic.

Cytotoxicity of the solution nitride samples was evaluated using MC3T3-E1 murine calvaria osteoblasts-like cells. The cell line was acquired from an authorized cell and gene bank (Riken Cell Bank, Ibaraki, Japan). The cells were grown and maintained in α minimum essential medium (α -MEM) supplemented with 1 % kanamycin and 10 vol.% fetal bovine serum in a humidified incubator with 95 % air and 5 % CO_2 at $37 \text{ }^\circ\text{C}$. Passaging and preparation of single cell suspensions for seeding on the metallic samples was achieved by enzymatic digestion using 0.25 vol.% trypsin, 0.02 % (w/v) EDTA solution in PBS at pH 7.4. Cells counts were performed using a Tatai-type hemacytometer under an inverted microscope. In vitro cytotoxicity was assessed by direct contact method. Disc-shaped specimens with approximate thickness of 1 mm and diameter of 10 mm were obtained from the nonporous alloys rods using electric discharge machining. Prior to cytotoxicity testing, each specimen was ground with 2000 grit SiC paper and ultrasonically cleaned with alcohol, and then rinsed in distilled water. Subsequently, the discs were autoclaved at $121 \text{ }^\circ\text{C}$ for 0.9 ks.

Cells were incubated at $37 \text{ }^\circ\text{C}$ in a humidified 5 % CO_2 atmosphere for 3- and 7-day intervals without renewal of the culture medium. The cells were examined under optical microscope and photographed with a Nikon DS-L2 color digital camera. The total cell number was analyzed after staining using digital image analysis. The measurements of the cell spreading area were analyzed at the different culture intervals and normalized to the maximum area available in the metallic surfaces. Cell proliferation and the assessment of extent of spreading and cell morphology assays were repeated four times. After 3 days of proliferation assays, media from the cells cultured with metallic materials were saved in quadruplicate for inductively coupled plasma (ICP) analysis.

Cytotoxicity testing of surgical implant materials is an important way to verify their biocompatibility. The quantitative results of the proliferation test obtained with the image analysis software are presented in Fig. 10.24 [26].

The cells cultured for 7 days multiplied actively on the four stainless steel surfaces compared to those cultured for 3 days. After each culture period, cells grown on stainless steel surfaces displayed a significantly lower proliferation rate than the cells cultured on type IV collagen-coated cell culture dish. One-way ANOVA showed no statistically significant difference for the cell numbers of four stainless steel samples after 3 and 7 days of culturing. In the case of pure Ni samples after 7 days in culture, the cell numbers were significantly smaller than that of four stainless steel samples and negative controls. While in the stainless steel

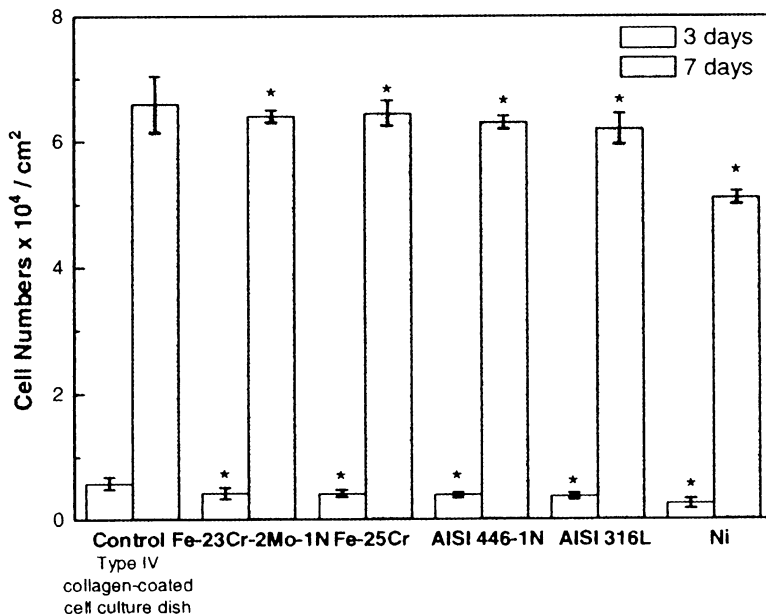


Fig. 10.24 Proliferation rates after 3 and 7 days in direct contact with the evaluated metallic materials with respect to the control cultures grown on type IV collagen-coated cell culture dish (100 %). (Reprinted with permission from [26] © 2008 Springer Science + Business Media, LLC)

surface cells proliferated forming multilayers after 7 days of culture, in the pure Ni sample, the formation of randomly located multilayer cell nodules was observed, indicating that the spreading was scarce and not uniform.

Morphology of adherent cells after 3-day incubation period is shown in Fig. 10.25. Microscopic analysis of the cell monolayers revealed that there were no notable differences in cell morphology between the type IV collagen cell culture dish (Fig. 10.25c) and the stainless steels (Fig. 10.25a–h). The body of osteoblasts has a mean size of 15 μm and many of them developed armlike cytoplasmic extensions with lengths up to 25 μm . MC3T3-E1 cells seemed to adhere tightly to surface under high magnification (750 \times magnification) (Fig. 10.25e–h) in accordance with the flattened morphology surrounded by cytoplasmic prolongations. MC3T3-E1 osteoblasts cells proliferated uniformly on the surface of Ni-free stainless steels under optical microscope (100 \times magnification) (Fig. 10.25a–d). Microscopic analysis of the cell cultures on pure Ni samples revealed that the cell morphology was altered. Cells grown on pure Ni exhibited reduced cytoplasmic area and also abnormally large cells (giant cells) were observed in both cultivation periods (Fig. 10.26).

After 3 days of culture, the MC3T3-E1 cellular spreading was good in all the evaluated stainless steel surfaces but not as extensive as in the cell culture dish treated with type IV collagen, and after 7 days of culture, osteoblasts were evenly

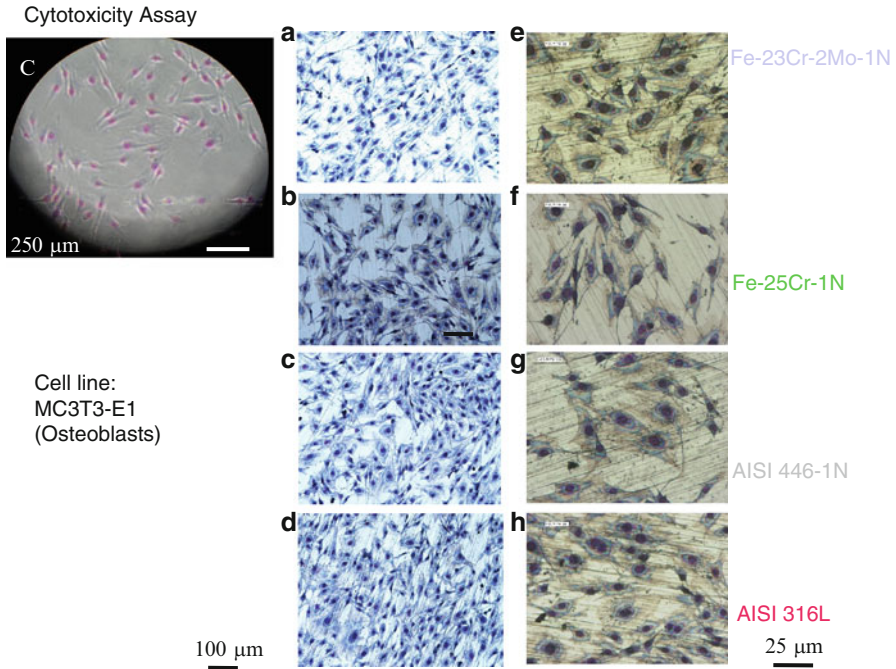


Fig. 10.25 Representative optical microscopy images of spread MC3T3-E1 osteoblasts cells after 3 days of direct cultivation on (C) type IV collagen-coated cell culture dish (a) and (e) Fe-23Cr-2Mo-1N, (b) and (f) Fe-25Cr-1N, (c) and (g) AISI 446-1N, and (d) and (h) AISI 316L. MC3T3-E1 cells are approaching confluence and display normal morphology. Original magnification: (C)15 \times , (a–d) 100 \times , (e–h) 750 \times (Reprinted with permission from [26] © 2008 Springer Science + Business Media, LLC)

spread covering the entire available stainless steel surfaces. Statistically significant difference between the average area of cells cultivated on the Ni-free stainless steel samples and AISI 316L samples was not observed.

10.5.2 *In Vivo* Osteocompatibility of Lotus Ni-Free Stainless Steel

A new generation of stainless steels, called nickel-free austenitic stainless steels, does not contain any nickel or the amount of nickel is very reduced (<0.5 wt%) [27], and those have been developed to be used in biological systems. The high nitrogen content is the reason of their superior corrosion resistance and elevated mechanical properties, and these advantages have been widely reported in the literatures [28]. As for the mechanical properties are concerned, the stiffness of

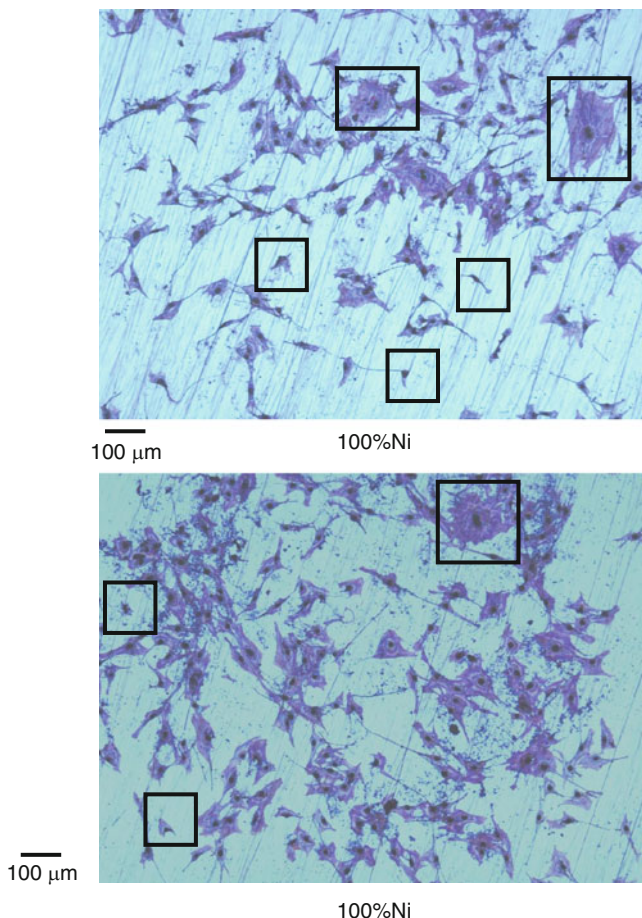


Fig. 10.26 Optical microscopic images of MC3T3-E1 osteoblast cells grown on pure Ni samples. A higher frequency of reduced cytoplasmic area cells and giant cells was observed (Reprinted with permission from [26] © 2008 Springer Science + Business Media, LLC)

stainless steels is far higher than that of compact bone, and this can lead to stress shielding to the host bone, which may result in detrimental resorptive bone remodeling. Moreover, high elastic moduli of stainless steel implants can cause delayed callus formation and bone healing. However, in order to solve this problem, a number of fabrication processes to produce porous bulk metals and alloys, including stainless steels, have been developed.

The introduction of pores into a structural material will drastically change its mechanical properties of stiffness, strength, and fatigue resistance. Moreover, the geometric microstructure of the porosity is able to change the physical properties such as specific surface area, apparent density, and degree of anisotropy. Based on clinical outcomes and histological evidence, the advantages of porous biomaterials

for bone–implant applications are multifold. Bone ingrowth is possible, which could greatly improve the bone–implant interface and may allow for efficient soft tissue attachment supplementing the stability of the implant by biological fixation. A strong bone–implant interface reduces harmful tissue strain and micromotion and therefore promotes the osseointegration of the implant, which is a basic requirement for its successful functioning as host organism. Additionally, by increasing the porosity of the implant material, its stiffness decreases correspondingly, reducing the stress-shielding effect, which can lead to resorption of the bone and the loosening of the implant.

For many clinical situations, a metallic porous graft offers structural integrity. These porous structures must provide temporary support and bone ingrowth. The greatest application fields are in the osseous reconstructive surgery, such as treatment of small bone defects, cranio-maxillofacial reconstruction, tooth root replacements, and vertebral body replacement. In applications in which a porous structure bridges gaps in tissues, the success of bone ingrowth is affected by the pore structure characteristics, such as pore density; pore orientation along length, width, or radial direction; pore size; and pore spacing. New porous metallic structures have to be developed to help advance the current generation of metallic grafts and address unresolved clinical applications. The evaluation of the bone apposition rates within differently oriented pores is also necessary in order to accomplish an efficient implant design.

Alvarez et al. [29] produced a lotus nickel-free austenitic stainless steel with longitudinally oriented pores by continuous zone-melting technique. In the former section, lotus structure was tested *in vivo* in a canine model achieving excellent bone ingrowth. This section describes further and detailed evaluation of lotus nickel-free austenitic stainless steel as a biomaterial candidate for the treatment of osseous defects and osseous reconstructive repairs in persons with strong nickel allergy predisposition.

The lotus rods of AISI 316L and AISI 446 were fabricated using the continuous zone-melting technique. AISI 316L is commonly used in biomedical applications and was selected as a reference material. AISI 446 stainless steel is a ferritic-type stainless steel that contains 0.3 wt% Ni as impurity. Sixty male, 8 weeks of age Sprague–Dawley rats, received bilateral femoral and tibia transcortical implants. In each femur and tibia, one sterile implants of the same alloy was carefully placed into the defect with the pores parallel or perpendicular to the long axis of the rat bone using a sterile forceps (Fig. 10.27). Animals were placed in pairs in cages and were given free access to food and water. The rats were sacrificed by ether suffocation. The left and right tibia bones were retrieved at 4, 8, and 12 weeks after implantation for histology analysis. The femurs also retrieved at 4, 8, and 12 weeks were reserved for mechanical testing. Twenty rats were used for each implantation period.

Push-out testing was performed after 4, 8, and 12 weeks postoperatively by applying a longitudinal compressive force to the cylinder implants. Schematic diagram for testing shear bonding strength between bone tissues and the implant is shown in Fig. 10.28. Push-out testing of the bone–implant samples was

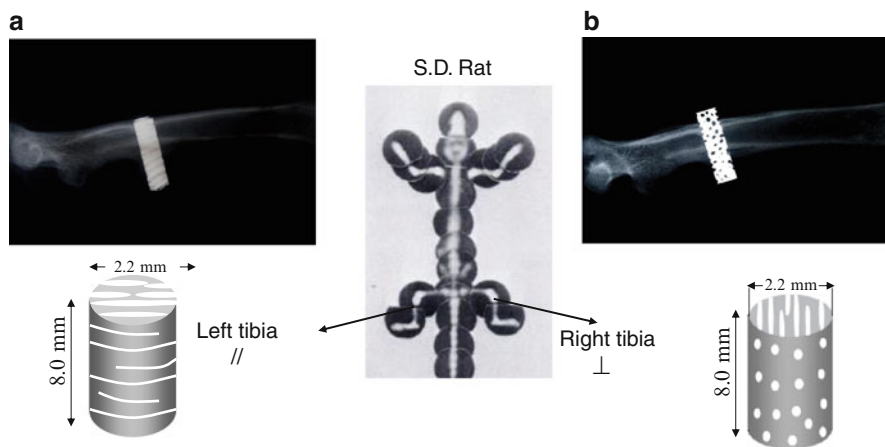


Fig. 10.27 Radiographs showing the implant placement configuration. (a) The elongated direction of the pores of the implant was parallel to the long axis of the rat bone. (b) The elongated direction of the pores of the implant was perpendicular to the long axis of the rat bone

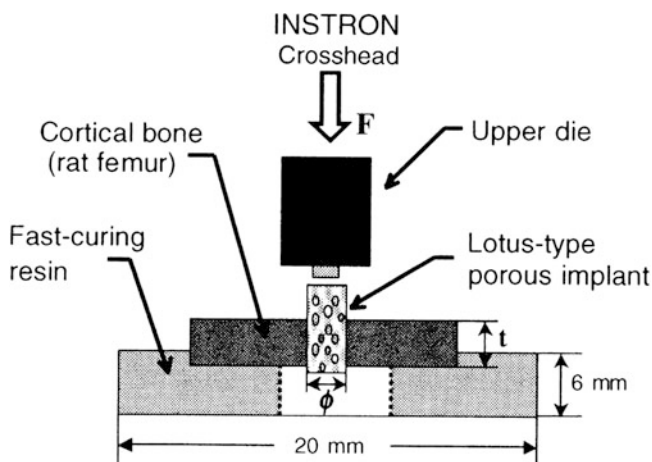


Fig. 10.28 Schematic diagram of the arrangement used for the mechanical push-out tests. F force applied on implant, t thickness of the cortical bone surrounding the implant, ϕ implant diameter (Reprinted with permission from [29] © 2008 Elsevier B.V.)

performed by using an INSTRON 4482 universal testing machine. The crosshead speed was set at 0.5 mm min^{-1} and the cylinder implants were tested to failure.

Signs of almost complete repair were observed with both types of implants. Histological evaluations revealed bone ingrowth even in the most central part of the lotus implants. Photomicrographs of representative histologic sections after 12 weeks implantation are shown in Fig. 10.29. At 12 weeks the histological

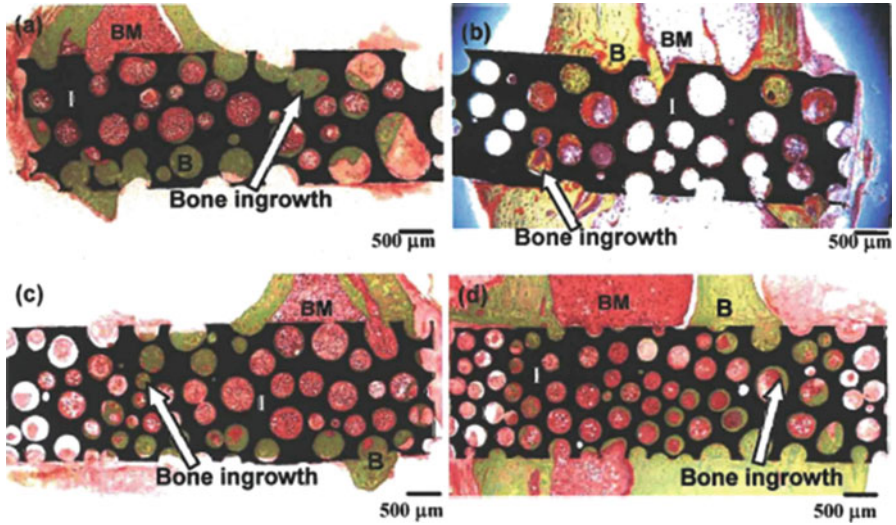


Fig. 10.29 (a) Lotus-type porous AISI 316L implant inserted with the elongated direction of the pores parallel (//) to the tibia bone long axis direction. (b) Lotus-type porous AISI 316L implant inserted with the elongated direction of the pores perpendicular (\perp) to the tibia bone long axis direction. (c) Lotus-type porous AISI 446-IN implant inserted with the elongated direction of the pores parallel (//) to the tibia bone long axis direction. (d) Lotus-type porous AISI 446-IN implant inserted with the elongated direction of the pores perpendicular (\perp) to the tibia bone long axis direction. Light microscopy histological sections after 12 weeks of implantation stained with Villanueva-Goldner's-Trichrome. (Reprinted with permission from [29] © 2008 Elsevier B.V.)

sections displayed an increase of bone contact and bone ingrowth. Indeed, it was found in many histological sections that the area of bone ingrowth within the implant surface was almost complete at 12 weeks. At higher magnifications, the fabricated implants demonstrated healthy cortical bone directly interfacing with the metallic materials (Fig. 10.30). The concept of bone–implant contact (osseointegration) is based on the light microscopic appearance of the biological side of the interface. Osseointegration implies an interface with remodeled, viable bone in direct contact with the implant surface, with no interposed fibrous tissue membrane. This study showed that osseointegration can be attained regularly after 12 weeks implantation time. In the lotus nickel-free implants, the mean bone ingrowth distance through the porous graft was 1,000 μm at 12 weeks, and the appearance of the host cortical bone located far from the implants was similar to the newly ingrown bone inside the pores.

Differences in bone ingrowth between AISI 316L and AISI 446-IN implants are presented in Fig. 10.31. In general, the amount of newly mineralized bone and the bone ingrowth distance into the implants progressively increased with time and maximum bone ingrowth was noted by 12 weeks. The results for both implant types showed that the alignment of the pores parallel (\parallel) to the bone long axis permitted a higher percentage of bone ingrowth. Histological analysis and computer-assisted

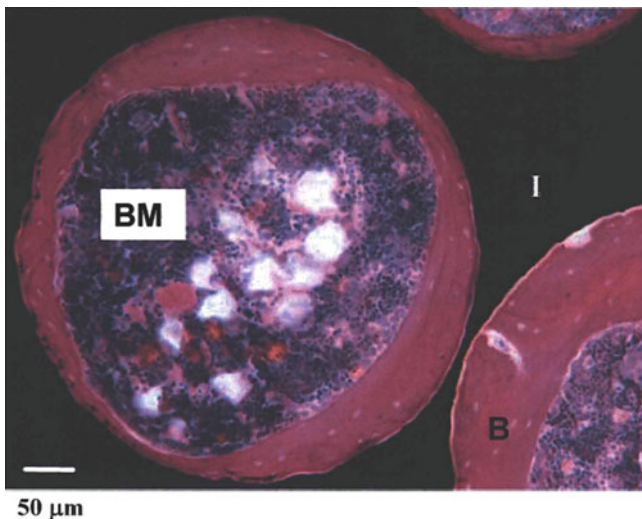


Fig. 10.30 Higher magnification light micrograph showing bone formation in apparent close contact with lotus AISI 446-1N Ni-free stainless steel at the internal part of the implant. Bone is stained pink, bone marrow purple, and Ni-free stainless steel is observed in black. Bar, 50 μm (Reprinted with permission from [29] © 2008 Elsevier B.V.)

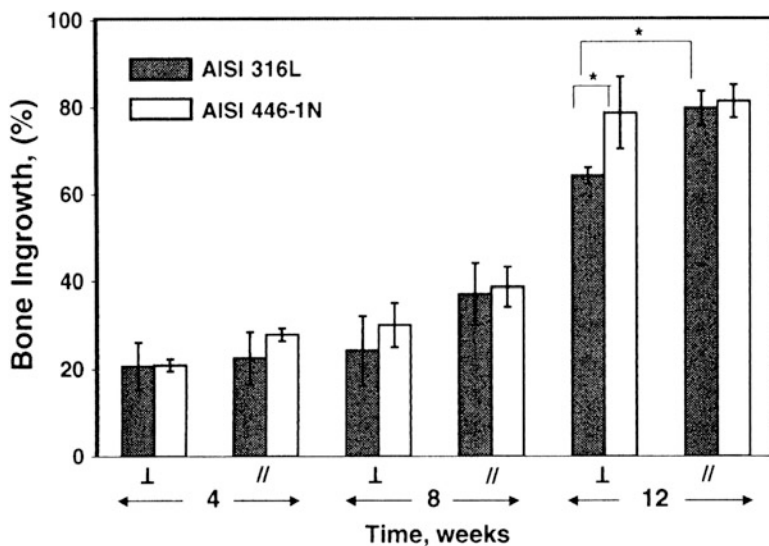


Fig. 10.31 Percentage of the newly formed bone in the total available pore space in the region of interest for lotus AISI 446-1N Ni-free stainless steel and lotus AISI 316L implants. // and \perp indicate parallel and perpendicular pore orientation with respect to the tibia long axis, respectively (Reprinted with permission from [29] © 2008 Elsevier B.V.)

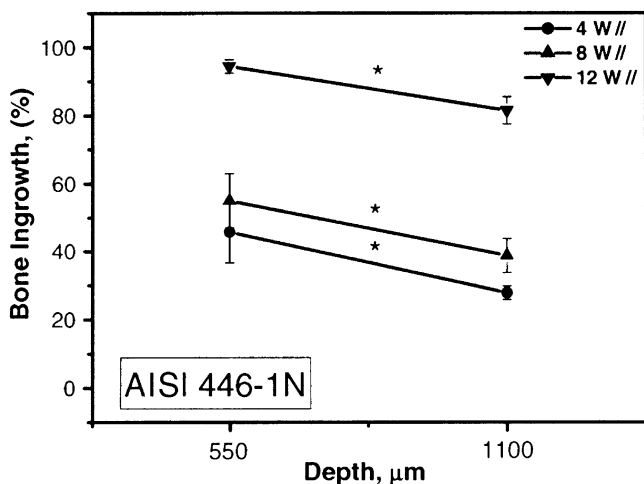


Fig. 10.32 Changes in the bone ingrowth as a function of the depth for each implantation period for lotus AISI-1N Ni-free stainless steel implants inserted with the elongated direction of the pores parallel with respect to the tibia long axis (Reprinted with permission from [29] © 2008 Elsevier B.V.)

quantification of the bone growth formed revealed that the bone formation within lotus AISI 446-1N had already reached in average 27.9 and 20.9 % after 4 weeks in the implants inserted parallel (\parallel) and perpendicular (\perp) to the bone axis direction, respectively. On the other hand, for lotus AISI 316L by 4 weeks, newly formed bone was 22.5 and 20.6 % in the implants inserted parallel and perpendicular to the bone long axis direction, respectively. Between the two types of materials, no statistically significant differences were noted with respect bone ingrowth.

To determine how deep the bone grew inside the lotus implants, bone ingrowth was determined from two consecutive histological sections. The bone ingrowth parameter was then examined as a function of depth into the implant. For lotus AISI 446-1N implants, these results are presented in Fig. 10.32. The bone ingrowth decreases with increasing depth into lotus implants. After 12 weeks in the middle of the implants, 82 and 79 % of bone ingrowth were obtained when the implants were inserted with the elongated direction of the pores oriented parallel or perpendicular to the tibia bone long axis direction, respectively.

Mechanical testing was performed since higher bone apposition does not necessarily imply greater bone-bonding strength. The applications of compressive shear forces at the bone-implant interface are a useful means of distinguishing bone-bonding quality and bone contact at the interface. Changes of bonding strength between bone tissues and the implants with the AISI 316L stainless steels are shown in Fig. 10.33. During the push-out tests, all the implants failed through the interface of implant and bone, and two specimens were broken on the bone side. For both alloys, the shear strength of the interface between bone and implants increased with an increase of the implantation time during the first 8 weeks, and this could be

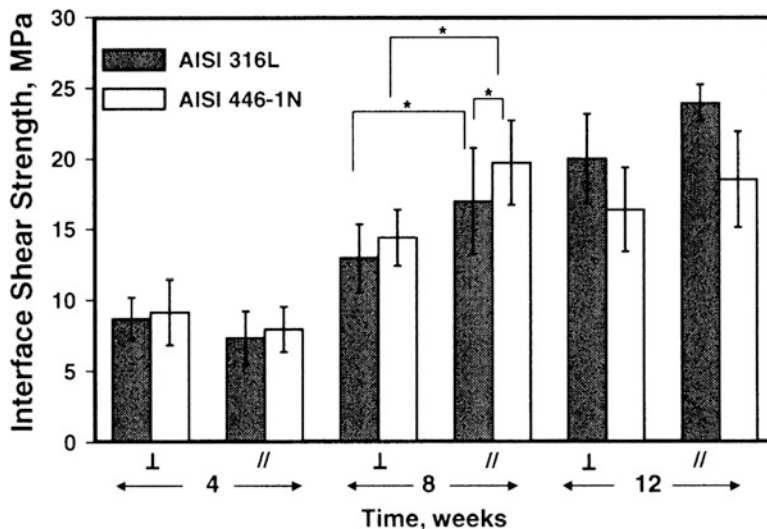


Fig. 10.33 Changes in the interface shear strength between the rat femur bone and the lotus implants with the implantation time. // and ⊥ indicate parallel and perpendicular pore orientation with respect to the tibia long axis, respectively (Reprinted with permission from [29] © 2008 Elsevier B.V.)

attributed to the increasing with time of the extent of penetration of new bone across the full diameter of the implants.

Although there were no significant differences among the 12 weeks strength values, maximum interfaces shear strength of approximately 22 ± 3 and 24 ± 1 MPa for lotus AISI 446-1N and lotus AISI 316L, respectively, were obtained at 12 weeks, and these values differed significantly from those of the 4 weeks group. When comparing in the literatures the failure loads of nonporous (smooth or rough surface) and porous-coated metallic implants with the failure loads of lotus implants, it turned out that the strength of bone–implant bonding of the fabricated lotus implants is about ten times higher than in porous-coated or nonporous metallic implants. According to the high shear forces needed to loose the implants at the interface, it is concluded that fabricated lotus implants provide tight fixation offering adequate pore volume for bone ingrowth.

10.5.3 *Biocompatibility of Lotus Stainless Steel and Titanium in Alveolar Bone*

Metallic materials for artificial hip joints, femoral heads, and metal plates to fix fragments are too strong and heavy for elderly patients, causing wear of the patients' bones, damaging and fracturing metals. In dental implantology,

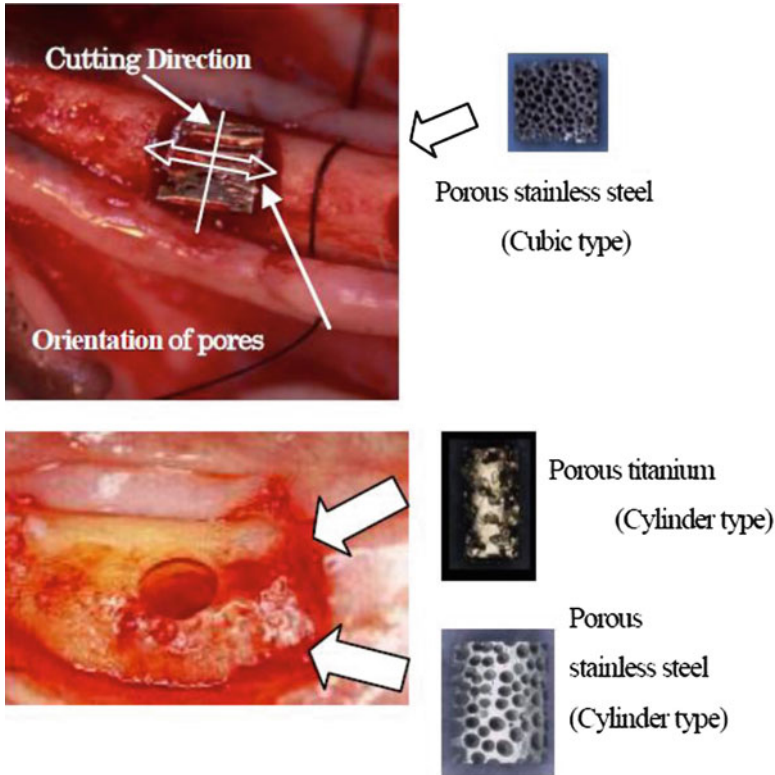


Fig. 10.34 Insertion of lotus metals to alveolar bone (Reprinted with permission from [32] © 2006 WILEY-Verlag GmbH & Co.)

insufficient trabecular bones contribute to poorer clinical results. It is due to insufficient bone–metal contact. One of the solutions to this phenomenon is the use of porous metallic materials. In natural teeth, Sharpey’s fibers make bundles to go into cementum. Minute pores of the cementum work as scaffold to another fiber bundles. The fiber bundles then resist vertical, lateral, and torsional stresses applied on the teeth [30]. The biomaterials with 150–200 μm pores are confirmed to facilitate bone ingrowth [31] and there exists a possibility to further improve functionality of the biomaterials. The conventional manufacturing technology, however, did not control shape and size of the pores so as to maintain certain mechanical strength. Higuchi et al. paid special attention to lotus metals whose pore size and orientation are controlled by utilizing gas pressure to investigate the biocompatibility of lotus stainless steel and titanium in alveolar bone in order to investigate the possibility of an implant by animal experiments [32].

Ten 5-year-old beagle dogs were used in this animal experiment. The dogs were under general anesthesia with intravenously injected pentobarbital sodium. The mandible premolars were extracted. When bone healing was obtained after three months, epithelial mucosa was stripped at the mandible premolars to expose

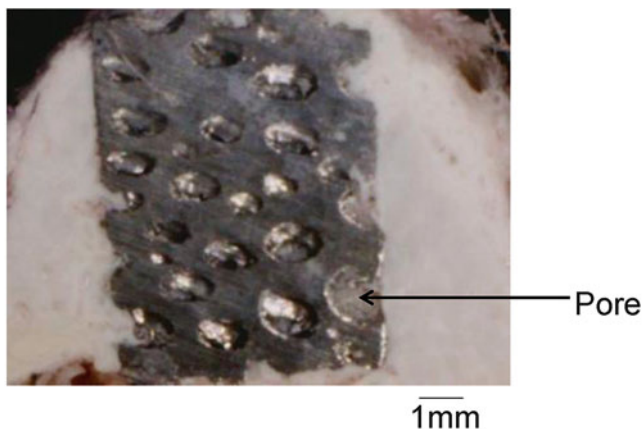


Fig. 10.35 Osteogenesis in the lotus stainless steel. Observed with actual condition by optical microscope after 4 weeks (Reprinted with permission from [32] © 2006 WILEY-Verlag GmbH & Co.)

mandibular bone. The cortical bone was drilled with a round bur under saline irrigation to create the implantation holes as shown in Fig. 10.34. The lotus metal samples were then implanted and the tissue was sutured. The samples were placed so that the pore direction is mesio-lateral to the mandibular bone. If the pore direction is buccolingual, the openings of the pores will contact the cortical bone, making it difficult to have active tissue ingrowth into the pores. The dogs were fed with water and pellet feeds for 2, 4, and 8 weeks before being sacrificed. At the end of the study period, the dogs were sacrificed with overdose of anesthetics. The specimens were observed with actual condition microscope, optical microscope, and SEM.

As a result, newly formed bones were not observed in lotus stainless steel SUS 304L after 2 weeks. In 4 weeks the active osteogenesis was observed on the surface of the pores as shown in Fig. 10.35, and it advanced into the depth of the pores in 8 weeks. Angiogenesis was rapid in cancellous bones and slower in cortical bones as shown in Fig. 10.36. After 4 weeks the sinusoidal vessels in porous dehydrogenated titanium formed dense vascular plexus advancing into depth of the pores (Fig. 10.37). Osteogenesis was identified in as early as 2 weeks. Osteogenesis was confirmed in the pores both after 4 and 8 weeks as shown in Fig. 10.38.

There is a technical problem to fabricate lotus titanium with uniform porosity and pore size like stainless steel. Living tissues, however, actively grew into the pores. In 2 weeks, active formation of vessels was observed around the metal with invasion into the pores, which was not observed in lotus stainless steel. In 4 weeks the sinusoidal vessels were developed into dense plexus, entering into the deep area of the pores. It is the same with osteogenesis. Newly formed bones were observable in 2 weeks. Pores were filled with new bones in 4 weeks. High biocompatibility of titanium seemed to include new bone formation without induction materials. Biocompatibility of titanium includes excellent cell adhesion property and

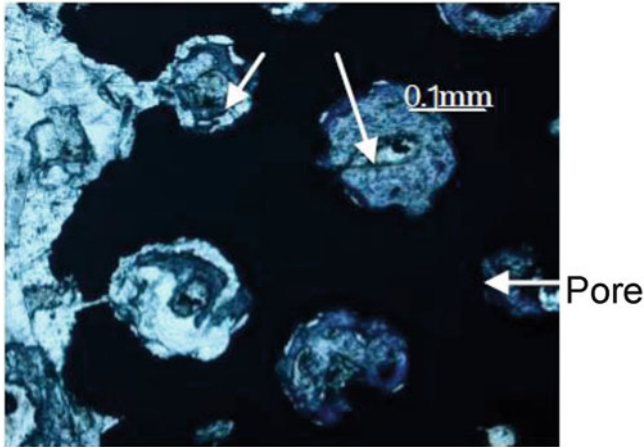


Fig. 10.36 Osteogenesis in the lotus stainless steel. Staining with triduin blue after 8 weeks (Reprinted with permission from [32] © 2006 WILEY-Verlag GmbH & Co.)

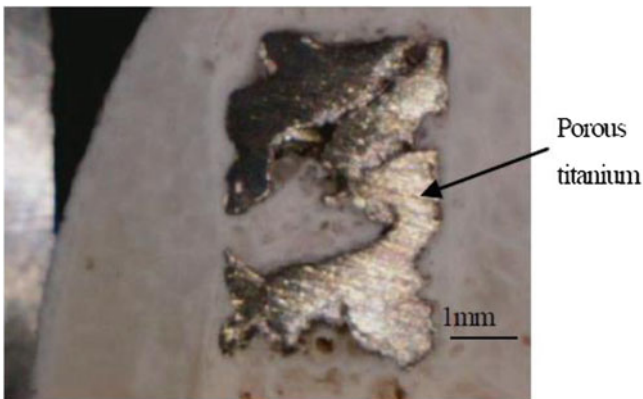


Fig. 10.37 Osteogenesis in porous titanium. Observed with actual condition by optical microscope after 4 weeks (Reprinted with permission from [32] © 2006 WILEY-Verlag GmbH & Co.)

biomineralization or the ability to deposit hydroxyapatite-like calcium phosphate on the surface under the presence of body fluid. The cells thus strongly adhered to the titanium surface release extracellular matrix to form scaffold for tissue formation. The vessels go into the pores along the scaffold, forming network earlier than lotus stainless steel. Early formation of capillary vessels allows early migration of osteoblasts in the porous titanium. Combination of osteoblasts and biomineralization [33] provides titanium better osteogenic environment than stainless steel. Though titanium is a metal, it has tissue compatibility equal to that of ceramics. One of the reasons for this is that titanium is easily oxidized and covered with an oxide layer. Exposure of titanium to body fluid through this oxide layer was

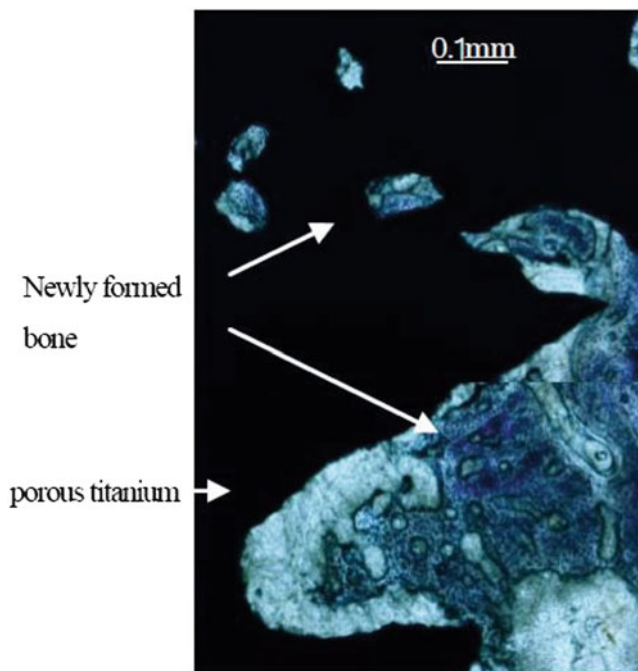


Fig. 10.38 Osteogenesis in porous titanium. Staining with truiduin blue after 8 weeks (Reprinted with permission from [32] © 2006 WILEY-Verlag GmbH & Co.)

considered to be causing ceramic-like behavior. Recently, however, it was found that immersion of titanium in body fluid-like solution produced the layer of hydroxyapatite. This phenomenon was not observed in gold alloy, gold–silver–palladium alloy, cobalt–chromium–nickel alloy, nickel–chromium alloy, or in stainless steel alloys. Furthermore, deposit on the Ti-6Al-4V or on Ti-50Ni alloy is not apatite. Higuchi et al. [33] conducted in vitro study that extracellular matrix became more absorbable to titanium through Ca ions. The favorable environment for extracellular matrix adsorption via Ca ion is thus created around the implant surface. Extracellular matrix formed in the tissue around titanium makes barrier to through extracellular matrix increases physical resistance, contributing to the initial fixation of titanium implants.

Regenerative medicine using cell proliferation has been the topic of research recently. It takes long time, however, before this technique becomes a mainstream due to such problems as carcinogenicity, ethical issues, complicated culture operation, and high cost. Scaffold for cell proliferation is indispensable for living tissue architecture in the regenerative medicine. The materials currently used are conventional biomaterials. Such hard tissue as bones and teeth needs to have stress resistance. It is highly expected to develop better combination of stiff biomaterials such as lotus metals and regenerative medicine for tissue repair. Development of artificial bones (Fig. 10.39) and joints of metals and ceramics has been active reconstruct structure supporting body and interlocking with joints.



Fig. 10.39 Parenchymatous defect of the mandible and biomaterial (Reprinted with permission from [32] © 2006 WILEY-Verlag GmbH & Co.)

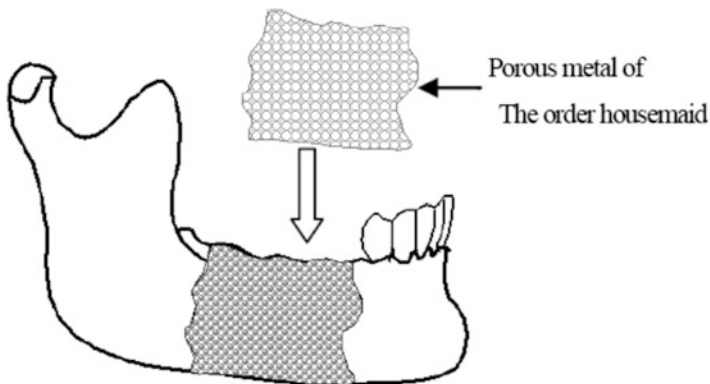


Fig. 10.40 Application of lotus metal for parenchymatous defect of the mandible (Reprinted with permission from [32] © 2006 WILEY-Verlag GmbH & Co.)

Metals have been used as biomaterials since it has sufficient stiffness to resist stress concentration fracture. Bones bear body weight, the stress of which acts as stimulus for repetitive remodeling. Remodeling is important in maintaining trabecular structures. Long implantation of stiff metals in the bone reduces stimulus to the adjunct bone, causing disuse atrophy. The challenge for the future is to make metal stiffness close to that of the bone (elastic modulus: 7–30 GPa). The lotus materials allow porosity control, giving metals elasticity. It is one of the ways to provide artificial materials with elastic modulus similar to bone modulus (Fig. 10.40). Porous metals with pore of 150–200 μm are said to be ideal for



Fig. 10.41 In the implant case, the bone resorption in maxilla mandible posterior is remarkable (Reprinted with permission from [32] © 2006 WILEY-Verlag GmbH & Co.)

artificial bones. The pores allow ingrowth of vessels and bones in the pores. They have a potential to develop into artificial bones with bone marrow, which is the final goal.

The implants allow contact between the metal and the gingiva. Absence of fibrous connection makes it more probable that bacteria and food residues enter from peri-implant space. Without more careful cleaning after implantology treatment, patients will experience peri-implant inflammation, which may be the cause of implant removal. Implants are composed of three components: super structures, fixtures, and abutment going through mucosa. Greatest difference between dental implants and other biomaterials is that implants communicate with *ex vivo* environment. Biomaterials other than dental implants are implanted inside the body, giving little opportunity for external bacteria coming into the body. Dental implants, on the other hand, are easily exposed by external bacteria. It is the reason why we have to make thorough oral care.

It has been impossible or less successful to use conventional dental implants for bones with compromised volume or osteoconduction (Fig. 10.41). Lack of fibrous connection gives no buffer against occlusive impacts, reducing abutment–mucous membrane connection. Porous implants should be developed to solve issues we currently face. There are several ways to manufacture porous implants: metal deposition onto fixture surface under high temperature and deposition through melting metal beads and fixture surface. The manufacturing process of porous implants with high functionality will allow to create pores in fixtures without depositing metal beads.

Lotus stainless steel and titanium can be utilized to create pores of 150–200 μm . It will allow growth of bony tissues alone in the pores to enhance holding force. Pore size can be controlled to 10 to 20 μm to allow fibers alone to come into the pores to add buffer against stress. Tailor-made many different types of implant can

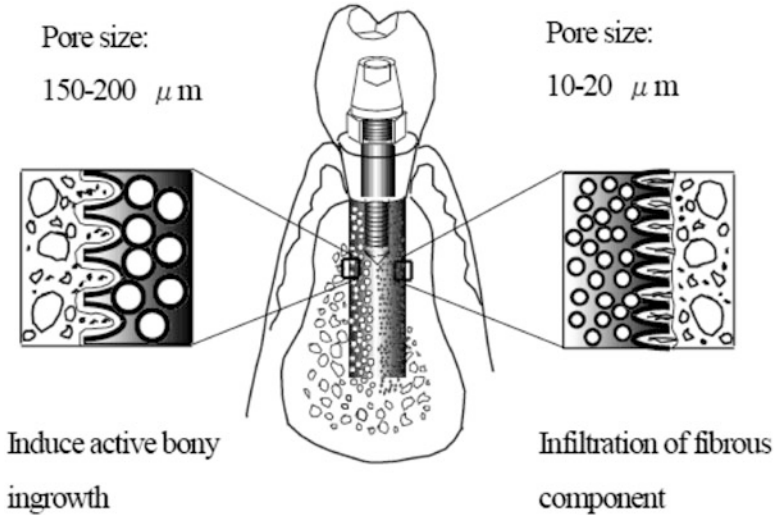


Fig. 10.42 Serve as basis for bone and fibrous tissue regeneration (Reprinted with permission from [32] © 2006 WILEY-Verlag GmbH & Co.)

be produced. Some can have strongly physical connection by fibers at the site where body communicates with external environment. The lotus metals can be better controlled to improve implant functions (Fig. 10.42). Fixture pore size can be controlled to 150–200 μm to allow only bony tissue to come into the pores and to enhance holding force. The size can be decreased to 10–20 μm to allow only fibrous tissue to come into pores, thus adding buffer to the stress. The fibrous connection is applied at the site of communication between implants and the external environment, enhancing physical binding strength. In the future the porous metals with porosity of 80 % can be used to tailor-made artificial bones.

References

1. Nishio S (2001) *J Thermal Eng. Jpn Soc Mech Eng* 617–622
2. Wei X, Joshi Y (2004) *J Electron Packaging* 126:60–66
3. Bastawros AF, Evans AG (1999) *ASME EEP (Am Soc Mech Eng Electronic Packaging Div)* 1:733–736
4. Hunt ML, Tien CL (1988) *Int J Heat Mass Trans* 31:301–309
5. Kamiuto K, Yee SS (2005) *Int Comm Heat Mass Trans* 32:947–953
6. Zhang HY, Pinjala D, Joshi YK, Wong TN, Toh KC, Ilyer MK (2004) *Proceedings of IEEE ITherm 2004*, pp 640–647
7. Chiba H, Ogushi T, Nakajima H, Ikeda T (2003) *JSME J Series B—Fluids Thermal Eng* 47:5843–5847
8. Chiba H, Ogushi T, Nakajima H (2011) *Proceedings of ASME/JME 2011 8th thermal engineering joint conference*, 13–17 March, Honolulu, ATTEC2011-44108

9. Shah RK, London AL (1978) *Advances in heat transfer series, Suppl 1*. Academic, New York, pp 192–197
10. Shah RK, London AL (1978) *J Fluids Eng* 100:177–179
11. Chiba H, Ogushi T, Nakajima H (2010) *J Thermal Sci Tech* 5:222–237
12. Yoshida I, Monma D, Iino K, Otsuka K, Asai M, Tsuzuki H (2003) *J Alloy Comp* 355:79–84
13. Golovin IS, Sinning HR (2003) *J Alloy Comp* 355:2–9
14. Xie ZK, Tane M, Hyun SK, Okuda Y, Nakajima H (2006) *Mater Sci Eng A* 417:129–133
15. Ota K, Ohashi K, Nakajima H (2003) *Mater Sci Eng A* 341:139–143
16. Nakajima H (2007) *Prog Mater Sci* 52:1091–1173
17. Greiner C, Oppenheimer SM, Dunand DC (2005) *Acta Biomater* 1:705–716
18. Jee CSY, Ozguven N, Guo ZX, Evans JRG (2000) *Metall Mater Trans B* 31:1345–1352
19. Oh IH, Nomura N, Masahi N, Hanada S (2003) *Scr Mater* 49:1197–1202
20. Bram M (2000) *Adv Eng Mater* 2:196–199
21. Cameron HU, Lilliar RM, Macnab I (1976) *J Biomed Mater Res* 10:295–302
22. Bobyn JD, Toh KK, Hacking SA, Tanzer M, Krigier JJ (1999) *J Arthroplasty* 14:347–354
23. Galante J, Rostoker W, Lueck R, Ray RD (1971) *J Bone Jt Surg* 53A:101–114
24. Zhang X, Ayers RA, Thorne K, Moore JJ, Schowengerdt F (2001) *Biomed Sci Instrum* 37:463–468
25. Story BJ, Wagner WR, Gaisser DM, Cook SD, Rust-Dawicki AM (1998) *Int J Oral Maxillofac Implants* 13:749–756
26. Alvarez K, Hyun SK, Fujimoto S, Nakajima H (2008) *J Mater Sci Mater Med* 19:3385–3397
27. Speidel MO (2004). US Patent 6,682,582
28. Gavriljuk VG, Berns H (1999) *High nitrogen steels*. Springer, Berlin, pp 267–268
29. Alvarez K, Hyun SK, Nakano T, Umakoshi Y, Nakajima H (2009) *Mater Sci Eng C* 29:1182–1190
30. Sims MR (1984) *Connec Tissue Res* 13:59–67
31. Hulbert SF, Cooke FW, Klawitter JJ, Leonard RB, Sauer BW, Moyle DD (1973) *J Biomed Mater Res* 4:1–23
32. Higuchi Y, Ohashi Y, Nakajima H (2006) *Adv Eng Mater* 8:907–912
33. Higuchi Y, Takahashi K, Asai T, Murata Y (2001) *J Osaka Dent Univ* 35:83–86